



HAL
open science

Atomic force microscopy (AFM), transmission electron microscopy (TEM), and scanning electron microscopy (SEM) of nano-scale plate-shaped second phase particles

Ihor Sobchenko, Josef Pesicka, Dietmar Baither, Werner Stracke, Thomas Pretorius, Lifeng Chi, Rudolf Reichelt, Eckhard Nembach

► To cite this version:

Ihor Sobchenko, Josef Pesicka, Dietmar Baither, Werner Stracke, Thomas Pretorius, et al.. Atomic force microscopy (AFM), transmission electron microscopy (TEM), and scanning electron microscopy (SEM) of nano-scale plate-shaped second phase particles. *Philosophical Magazine*, 2008, 87 (17), pp.2427-2460. 10.1080/14786430701203184 . hal-00513818

HAL Id: hal-00513818

<https://hal.science/hal-00513818>

Submitted on 1 Sep 2010

HAL is a multi-disciplinary open access archive for the deposit and dissemination of scientific research documents, whether they are published or not. The documents may come from teaching and research institutions in France or abroad, or from public or private research centers.

L'archive ouverte pluridisciplinaire **HAL**, est destinée au dépôt et à la diffusion de documents scientifiques de niveau recherche, publiés ou non, émanant des établissements d'enseignement et de recherche français ou étrangers, des laboratoires publics ou privés.



Atomic force microscopy (AFM), transmission electron microscopy (TEM), and scanning electron microscopy (SEM) of nano-scale plate-shaped second phase particles

Journal:	<i>Philosophical Magazine & Philosophical Magazine Letters</i>
Manuscript ID:	TPHM-06-Sep-0365.R2
Journal Selection:	Philosophical Magazine
Date Submitted by the Author:	04-Jan-2007
Complete List of Authors:	Sobchenko, Ihor; University of Muenster, Materialphysik; Cherkasy, Theoretical Physics Pesicka, Josef; Charles University, Faculty of Mathematics & Physics Baither, Dietmar; University of Muenster, Materialphysik Stracke, Werner; Universitaet Muenster, Institut fuer Medizinische Physik und Biophysik Pretorius, Thomas; Universitaet Muenster, Materialphysik; Bremer Institut fuer angewandte Strahltechnik Chi, Lifeng; Universitaet Muenster, Physikalishes Institut Reichelt, Rudolf; Universitaet Muenster, Institut fuer Medizinische Physik und Biophysik Nembach, Eckhard; University of Muenster, Materialphysik
Keywords:	atomic force microscopy, nanoparticles, nanoscale precipitates, Ni-based superalloys, nickel alloys, phase decomposition, SEM, transmission electron microscopy
Keywords (user supplied):	magnetic force microscopy, superellipsoid, plate-shaped precipitates

1
2
3
4
5
6
7
8
9
10
11
12
13
14
15
16
17
18
19
20
21
22
23
24
25
26
27
28
29
30
31
32
33
34
35
36
37
38
39
40
41
42
43
44
45
46
47
48
49
50
51
52
53
54
55
56
57
58
59
60



For Peer Review Only

**Atomic force microscopy (AFM), transmission electron microscopy (TEM),
and scanning electron microscopy (SEM)
of nano-scale plate-shaped second phase particles**

**IHOR SOBCHENKO^{†§}, JOSEF PESICKA^{†+}, DIETMAR BAITHER[†],
WERNER STRACKE[#], THOMAS PRETORIUS^{†¶}, LIFENG CHI[×],
RUDOLF REICHEL[#], and ECKHARD NEMBACH^{†*}**

[†] Institut für Materialphysik, Universität Münster,

Wilhelm-Klemm-Strasse 10, 48149 Münster, Germany

[#] Institut für Medizinische Physik und Biophysik, Universitätsklinikum, Universität Münster,

Robert-Koch-Strasse 31, 48149 Münster, Germany

[×] Physikalisches Institut, Universität Münster,

Wilhelm-Klemm-Strasse 10, 48149 Münster, Germany

[§] Permanent address: Department of Theoretical Physics, Cherkasy National University,

Shevchenko Blv. 81, 18031 Cherkasy, Ukraine

⁺ Permanent address: Charles University, Faculty of Mathematics and Physics,

Department of Metal Physics, Ke Karlovu 5, 12116 Prague, Czech Republic

[¶] Now with: Bremer Institut für angewandte Strahltechnik,

Klagenfurter Strasse 2, 28359 Bremen, Germany

* Corresponding author. E-mail: nembach@nwz.uni-muenster.de

Phone: ++49-251-83-33570, Fax: ++49-251-83-38346

Abstract: The feasibility of accurately measuring the size and the volume fraction of nano-scale plate-shaped precipitates by atomic force microscopy (AFM) has been explored. For quantitative evaluations their unhandy geometry is conveniently described as superellipsoids. The experimental alloy Ni₆₉Co₉Al₁₈Ti₄ served as a model system: plate-shaped disordered γ -precipitates form in the L1₂-long-range ordered γ' -matrix. The results obtained by AFM are compared with those derived from transmission (TEM) and from high resolution scanning electron microscopy (SEM). The agreement between the AFM and the TEM results is good. In spite of the low number of SEM images taken, the same holds for

1
2 the SEM results. In addition, magnetic force microscopy was applied; its results are
3 acceptable. The main advantages of AFM are (i) the numerical output for all three
4 dimensions, (ii) the simplicity of its operation, and (iii) the lower cost of the microscope itself.

Formatted

5
6 The first point allows to directly subject the numerical AFM output data to automated
7 computer based evaluations. All present experimental and evaluation procedures are also
8 applicable to cube-shaped particles with rounded edges and corners as found e.g. in
9 γ' -strengthened nickel based superalloys.
10
11

12
13 *Keywords:* Atomic force microscopy (AFM); Magnetic force microscopy (MFM);
14 Transmission electron microscopy (TEM); Field emission scanning electron microscopy
15 (FESEM); Plate-shaped precipitates; Second phase particles; Nickel based alloy;
16 Nano-structure; Superellipsoid.
17
18
19
20

21 1. Introduction

22
23 Many structural materials derive their high strength from coherent precipitates of secondary
24 phases. Well known examples are Guinier-Preston zones in aluminium based alloys and
25 γ' -precipitates in nickel based superalloys [1-3]. The strengthening effects of coherent
26 precipitates are governed by their shape, size, and volume fraction and by intrinsic properties
27 of the two phases involved, e.g. by their crystal structure, their lattice mismatch, and their
28 elastic stiffness. The shape of the precipitates in turn depends on their specific interface
29 energy, their lattice mismatch, and the elastic stiffness of both phases. Anisotropies of these
30 parameters are of great importance. The most common shapes are spheres, cubes, and plates.
31 Plates are favoured by a low specific interface energy, a high lattice mismatch, a low elastic
32 stiffness of the precipitates, and a high precipitate volume [4-6]. In the case of spheres and
33 cubes their size is described by the average radius r and by the average cube length d ,
34 respectively. To characterise plate-shaped precipitates at least two parameters are required:
35 some linear measure $2a$ of their average areal extension and their average thickness $2b$. In
36 addition, the distribution functions Φ of the individual particle radius ρ_i , the cube length
37 δ_i , the areal extension $2\alpha_i$, and the thickness $2\beta_i$ are considered.
38
39
40
41
42
43
44
45
46
47

48 The size of precipitates relevant for strengthening is in the nanometer range; hence the
49 standard method for the determination of r , d , a , and b is transmission electron microscopy
50 (TEM). Since atomic force microscopes (AFM) are much easier to operate and of much lower
51
52

1
2 cost, more recently they too have been used to determine the size and the volume fraction of
3 spherical and cubic particles [7-13]. Moreover in contrast to the TEM, also compact
4 specimens can be investigated in the AFM, which facilitates the preparation of the specimens,
5 and thanks to the direct [three-dimensional](#) digital output automated computer based
6 evaluation procedures can readily be applied.
7
8
9

10
11 In two former investigations [11,12], the present groups successfully used AFMs for
12 the accurate determination of r , $\Phi(\rho_i)$, and the volume fraction of two different types of
13 *spherical* nano-scale second phase particles. Elaborate quantification procedures were
14 developed. Special attention had been paid to effects of the finite size of the AFM tip and to
15 the preferential attack of the matrix by the electrolyte. Presently the feasibility to characterise
16 *plate-shaped* precipitates by AFM has been explored. Their lower symmetry renders their
17 characterisation more involved because (i) the two lengths a and b instead of just one have to
18 be measured and (ii) the often high aspect ratio a/b complicates the choice of the
19 magnification. Good statistics necessitate the evaluation of a high number of particles. Hence
20 the relatively high value of a calls for a low magnification, whereas the smaller thickness b
21 calls for a high magnification. To verify the AFM results they are compared with results
22 derived from TEM and high resolution field emission scanning electron microscopy
23 (FESEM). Since the investigated material is ferromagnetic, also magnetic force microscopy
24 (MFM) was performed. For this purpose the standard AFM tips were replaced by hard
25 magnetic cobalt alloy coated ones. All experimental and evaluation procedures reported
26 below are also applicable to cube-shaped particles with rounded edges and corners; in this
27 case a equals b .
28
29
30
31
32
33
34
35
36
37

38 The experimental alloy $\text{Ni}_{69}\text{Co}_9\text{Al}_{18}\text{Ti}_4$ served as a model system. After ageing below
39 about 1380K, this alloy is two-phase: nano-scale coherent precipitates of the disordered or
40 short-range ordered f.c.c. γ -phase are embedded in the L1_2 -long-range ordered γ' -phase [14-
41 16]. Evidently this arrangement of phases is inverse to that of nickel based superalloys, in
42 which the γ -phase forms the matrix and particles of the γ' -phase precipitate [1-3].
43 Strengthening of $\text{Ni}_{69}\text{Co}_9\text{Al}_{18}\text{Ti}_4$ by γ -precipitates and the relevant dislocation processes were
44 the subjects of two former studies [15,16]. In fact, this alloy had been designed as a model
45 system for the investigation of particle strengthening of intermetallic phases. Since the former
46 specimens had been aged for up to 264h at 973K the γ -precipitates in them were very small
47 and of approximately spherical shape: r was below 7nm. The present specimens were aged for
48
49
50
51
52
53
54
55
56
57
58
59
60

333h at 1173K, which resulted in larger and hence plate-shaped γ -precipitates. TEM, FESEM, AFM, and MFM images are presented in section 4. The present γ' -phase may be considered as a derivative of the well-known intermetallic phase Ni_3Al [17]. The γ -precipitates are richer in Co and poorer in all other constituents than the γ' -matrix. This will be detailed in section 3.

After the nucleation process of γ -precipitates is accomplished, the growth of their average size is mainly governed (i) by further depletion of the γ' -matrix of Co and (ii) by dissolution of smaller γ -precipitates and incorporation of their material by bigger ones. The latter process is analogous to Ostwald ripening of spherical precipitates [18]: the total amount of interface energy is reduced. Pretorius et al. [15] aged $\text{Ni}_{69}\text{Co}_9\text{Al}_{18}\text{Ti}_4$ isothermally at 973K and found that for $r < 7\text{nm}$ the γ -volume fraction increased with ageing time.

Deleted: γ -forming elements

2. Crystallography and geometry of the γ -precipitates

The crystallography of coherent plate-shaped precipitates determines the optimum imaging geometry. The habit planes of the plate-shaped γ -precipitates in $\text{Ni}_{69}\text{Co}_9\text{Al}_{18}\text{Ti}_4$ are of the type $\{001\}$. Therefore the Miller indices of the plane of the thin TEM-foils were chosen to be (001) and the incident electron beam in the TEM and FESEM was normal to them. Other imaging geometries would have complicated the evaluations further. The two families of γ -plates with the indices (100) and (010) are imaged edge-on, whereas the (001)-family is viewed in-plane. The same foils were studied by the TEM, FESEM, and AFM. The morphology of the γ -precipitates is in accordance with the observation that Young's modulus of γ' -strengthened superalloys is lowest along $\langle 001 \rangle$ -directions [19,20].

'[insert figure 1 about here]'

The γ -precipitates are neither flat circular cylinders, nor flat cuboids, nor flat standard ellipsoids of revolution (see section 4), but they can be very well described as superellipsoids [21-26]. The coordinates of points on the $\gamma' - \gamma$ -interface of an (001)-in-plane γ -precipitate which is centred at the origin of the coordinate system, are

Deleted: 5

$$\left(\frac{|x|}{\alpha}\right)^n + \left(\frac{|y|}{\alpha}\right)^n + \left(\frac{|z|}{\beta}\right)^k = 1 \quad . \quad (1)$$

α and β are the half-axes with $\alpha > \beta$. The exponents n and k are integers exceeding 2.

Evidently the mathematical description of a superellipsoid involves four independent parameters. α appears in the denominator of $|x|$ as well as of $|y|$ because the extension of in-plane (001)- γ -plates is approximately the same in these two directions (see section 4).

Deviations from this symmetry will be discussed below and in section 4.1.2. For $n=k=2$ a standard rotational ellipsoid is obtained and for $n \rightarrow \infty$ and $k \rightarrow \infty$ a cuboid. The effects of n and k on the shape of the superellipsoid are demonstrated in figure 1 for $\alpha = 5\beta$. The

intersections of the superellipsoid with the plane characterised by $y \equiv 0$, i.e. edge-on view, and with the plane $z \equiv 0$, i.e. in-plane view, are shown in figures 1(a) and (b), respectively. The

quoted intersections are superellipses [25,26]. Figure 1(c) gives three-dimensional sketches for four combinations of n and k and thus visualises the effects of these exponents on the shape of the superellipsoid. For the volume V of the superellipsoid holds

$$V = q_V(n,k) \pi \alpha^2 \beta \quad . \quad (2a)$$

The subscript 'v' of the coefficient $q_V(n,k)$ indicates 'volume'. Some values of $q_V(n,k)$ are listed in figure 1(a). Equation (2b) is an approximate numerical representation of the function $q_V(n,k)$:

$$q_V(n,k) = a_0 + a_n n + a_{nn} n^2 + a_k k + a_{kk} k^2 + a_{nk} nk \quad (2b)$$

with $a_0=0.1404$, $a_n=0.4992$, $a_{nn}=-0.0383$, $a_k=0.2369$, $a_{kk}=-0.0158$, $a_{nk}=-0.0094$. For n and k between 2 and 6, this approximation is accurate within $\pm 2\%$ [25].

A generalisation of equation (1) is possible by allowing (i) for different lengths of the two longer half-axes and / or (ii) for different exponents, i.e. the first two terms in equation

(1) are replaced by $(|x|/\alpha_1)^{n_1}$ and $(|y|/\alpha_2)^{n_2}$, respectively, with $\alpha_1 \neq \alpha_2$ and / or $n_1 \neq n_2$

[25]. In this case also equation (2a) has to be modified

$$V = q_V(n_1, n_2, k) \pi \alpha_1 \alpha_2 \beta \quad . \quad (2c)$$

For later reference the average length $\sigma_\alpha(n)$ of chords through the superellipsoid are defined. The average is taken over chords which (i) lie in the (001)-plane (in-plane view) characterised by $z \equiv 0$ and (ii) are parallel to [010], i.e. $\sigma_\alpha(n)$ equals the average vertical extension of the sketches in figure 1(b):

$$\sigma_\alpha(n) = q_c(n,n) \alpha \pi \quad (3a)$$

The subscript 'c' indicates 'chord'. $q_c(n,n)$ equals: 0.5000, 0.5623, 0.5902, 0.6049, $2/\pi=0.6366$ for $n = 2, 3, 4, 5, \infty$, respectively [25]. $n = 2$ and ∞ refer to a circle and a square, respectively. Two more analogous average chords are defined: $\sigma_\beta(n,k)$, which refers to chords which (i) lie in the (010)-plane (edge-on view) characterised by $y \equiv 0$ and (ii) are parallel to [001], i.e. to horizontal chords in figure 1(a), and $\sigma_\alpha(n,k)$, which refers to chords which (i) lie in the (010)-plane (edge-on view) characterised by $y \equiv 0$ and (ii) are parallel to [100], i.e. to vertical chords in figure 1(a).

Deleted: 4

$$\sigma_\beta(n,k) = q_c(n,k) \beta \pi \quad (3b)$$

$$\sigma_\alpha(n,k) = q_c(n,k) \alpha \pi \quad (3c)$$

$q_c(n,k)$ is symmetric, i.e. $q_c(n,k)=q_c(k,n)$. Equation (3d) is a numerical approximation of the function $q_c(n,k)$; for n and k between 2 and 6, it is accurate within $\pm 1.5\%$:

$$q_c(n,k) = a_0 + a_n(n+k) + a_{nn}(n^2+k^2) + a_{nk}nk \quad (3d)$$

with $a_0=0.3573$, $a_n=0.0458$, $a_{nn}=-0.0028$, $a_{nk}=-0.0027$.

With the aid of equations (3b) and (3c) the area $\mathbf{A}(\alpha, \beta, n, k)$ of a superellipse which is characterised by the parameters α, β, n , and k , can be calculated

$$\mathbf{A}(\alpha, \beta, n, k) = 2\alpha q_c(n,k) \beta \pi \quad (3e)$$

Applying equations (1) – (3), all relevant geometric parameters of any type of convex particles, e.g. of cubes with rounded edges and corners, can easily be calculated: volume, area

1
2 of the particle / matrix interface, intersections of the particle with any crystallographic plane,
3 chords. The γ' -precipitates in the most advanced nickel based superalloys are such cubes [3,7-
4 9].
5
6

8 3. Experiments

10 Slices of 0.3mm thickness were spark cut from aged $\text{Ni}_{69}\text{Co}_9\text{Al}_{18}\text{Ti}_4$ -single crystals, ground,
11 and twin-jet electro-polished ([electro-polishing machine: Tenupol-3 \[Struers, Copenhagen,](#)
12 [Denmark\]; electrolyte: 20ml perchloric acid \(63%\) in 80ml ethanol; temperature: 240K;](#)
13 [voltage: 25V](#)). With the following two exceptions the preparation of the thin TEM-foils was
14 the same as in Refs. [15,16]: (i) the present ageing conditions were 333h at 1173K, which
15 resulted in plate-shaped, instead of spherical (see section 1) γ -precipitates, and (ii) the shape
16 and crystallography of the γ -precipitates required that the indices of the plane of the foils were
17 (001) (see section 2). The present ageing treatment was preceded by a γ -nucleation treatment:
18 24h at 978K. As described by Baither et al. [16], the aged material contained some widely
19 spaced irregular arrangements of the two phases. This was due to dendritic growth of the
20 single crystals. Since the spacing of these irregularities was around 0.3mm, they could easily
21 be avoided in the microscopes.
22
23
24
25
26
27
28
29

30 Without any additional preparation specific to the applied microscope, the same foils
31 were studied by TEM, FESEM, and AFM. All micrographs were taken at ambient
32 temperature. Two AFMs, AFM1 and AFM2, were used, both with two different types of tips,
33 Tip1 and Tip2. The TEM, the FESEM, and AFM1 were the same ones as in the previous
34 studies of spherical particles [12,16]. AFM1: AP-100 Autoprobe CP (Park Scientific
35 Instruments, Sunnyvale, USA); AFM2: DimensionTM 3000 (Digital Instruments, Santa
36 Barbara, USA); 200kV-TEM: 800NA (Hitachi, Tokyo, Japan); FESEM: S-5000 (Hitachi,
37 Tokyo, Japan). Tip1: SuperSharpSiliconTM (tip radius<5nm, typical \approx 2nm; half-cone angle of
38 the [outermost](#) 200nm of the tip <10°); Tip2: PointProbe[®] (tip radius<10nm, typical <7nm;
39 half-cone angle \approx 20°, but <10° at the very end of the tip). Both types of tips are produced by
40 NANOSENSORSTM, Neuchâtel, Switzerland, who also provided the quoted specifications.
41 The tip radii and the cone angles were checked by FESEM and TEM. TEM yielded the result
42 that for Tip2 the radius is indeed below 10nm and the half-one angle – measured over the
43 outermost 150nm – does not exceed 15°. Since Tip1 is very fragile, its first approach to the
44 specimen required utmost care. Both AFMs are constructed such that the tip of the monolithic
45
46
47
48
49
50
51
52
53
54
55
56
57
58
59
60

Deleted: last

1
2 cantilevers is inclined by 12° in AFM1 and by 10° in AFM2, away from the normal. Scans
3 were performed along two alternative orthogonal directions: from side to side and from front
4 to back. The quality of the topographs obtained was the same for both directions. The
5 magnifications of the microscopes were calibrated; hence possible remaining errors are
6 estimated to be at most 0.5% for the TEM, 2% for the FESEM, 2% for AFM1, and 5% for
7 AFM2.
8
9
10

11
12 FESEM and AFM revealed that the electrolyte attacks the γ -precipitates more strongly
13 than the γ' -matrix (see sections 4.2 and 4.3). Hence they appear as pits in the FESEM and
14 AFM images. In the following the pits left behind by the etched away parts of the
15 γ -precipitates will be referred to as γ -pits. The present etching effect is the same one as that
16 observed for nickel based superalloys, in which the γ -matrix was more strongly attacked than
17 the strengthening γ' -precipitates, which stuck out of the foils [12]. It is emphasised that
18 etching was not intended, but was a mere side effect of the standard electro-polishing
19 procedure of thin TEM-foils. Since the same specimens were to be studied in all three types
20 of microscopes ([TEM](#), [FESEM](#), [AFM](#)), the requirements of the TEM had to be fulfilled.
21
22
23
24
25
26
27

28 The present material $\text{Ni}_{69}\text{Co}_9\text{Al}_{18}\text{Ti}_4$ is ferromagnetic at ambient temperature. Hence
29 also magnetic force microscopy (MFM) could be performed: AFM2 was operated with a tip
30 of the type PointProbe-MFMR, which had a 40nm thick cobalt alloy coating. Its producer
31 NANOSENSORSTM specifies that the typical tip radius is less than 50nm. The preparation of
32 the specimens investigated by MFM was similar to that of those studied by the other
33 microscopes, but they were only mechanically ground and polished, finally with 250nm
34 diamond paste. There was *no* electro-polish and hence *no* etching. The root mean square
35 roughness measured by AFM2 equipped with a magnetic tip was less than 2.5nm.
36
37
38
39
40

41 While the TEM produces a parallel projection of the volume of the thin foil into a
42 plane perpendicular to the optical axis, the AFM and the FESEM yield three-dimensional
43 information on the surface profile of the foil and the MFM registers differences in magnetic
44 field above the surface. In the evaluations, allowances are made for the fact that even
45 γ -precipitates whose centres lie outside the thin foil, may yield contrast.
46
47
48
49

50 The compositions of both phases of the thin foils were determined by energy
51 dispersive X-ray (EDX) analyses in the TEM. The following atomic percentages were found
52
53

1
2 in the γ' - / γ -phase: Ni 68.6 / 65.1, Co 9.5 / 21.9, Al 17.8 / 12.5, Ti 4.1 / 0.5. The error limits
3 of these concentrations are estimated to be between 1 and 2at.%. In agreement with common
4 knowledge [e.g. 2, 27] Co preferentially partitions to the γ -phase and Al and Ti to the
5
6
7 γ' -phase.

Deleted: 6

9 10 **4. Data evaluations**

11 Since TEM, SEM, AFM, and MFM images require different evaluation procedures, the
12 respective analyses are presented in separate sections. The same holds for edge-on and
13 in-plane γ -particles. It is stressed that the planes of all micrographs, presented as well as
14 evaluated ones, are parallel to the (001)-plane of the TEM-foil. So far no automated computer
15 based evaluation procedure was implemented, because it would require the exact
16 standardisation of all processes. In routine work, however, such procedures are very helpful.

21 22 **4.1 Transmission electron microscopy**

23
24 The $L1_2$ -long-range ordered γ' -precipitates in superalloys are normally dark-field imaged with
25 one of their superlattice reflections. Due to the inverse arrangement of the γ - and γ' -phase in
26 $Ni_{69}Co_9Al_{18}Ti_4$ (see section 1), presently bright field images were taken. An example is
27 presented in figure 2. The standard magnification was 10,000 \times and the photographic
28 negatives were scanned with 600dpi. Four to ten scanned neighbouring original micrographs
29 were 'pasted together' in the computer and treated as one micrograph. The evaluation of each
30 pasted together micrograph started with a search for those γ -pits whose entire images were in
31 the micrograph. Subsequently the area A was delimited by straight lines such that the centres
32 of the 'entire' γ -images lay within A . Evidently some margins which contained partially
33 imaged γ -pits, were disregarded. Tracing out the evaluated area A involved some
34
35
36
37
38
39
40
41
42
43
44
45
46
47
48
49
50
51
52
53
54
55
56
57
58
59
60
arbitrariness, which is allowed for in the quoted error limits. The percentage of the respective
error decreases as A increases. Pasting together helped to use the original micrographs more
efficiently because fewer margins containing partially imaged γ -pits had to be disregarded.
Analogous procedures were applied to the FESEM, AFM, and MFM images. The thickness t
of the thin TEM-foils was determined by convergent beam electron diffraction. Within the
experimental limits of error of 10%, t was constant throughout each pasted together
micrograph. Six TEM-foils were studied; they yielded nine pasted together areas taken at
different parts of the foils. The same areas were evaluated for edge-on and for in-plane γ -pits.

Deleted:

1
2
3
4 [insert figure 2 about here]

5
6 Since the standard direction of the incident electron beam was along the highly
7 symmetric [001]-direction, many beams were excited. In order to study some finer details, a
8 few micrographs were taken under different conditions: (i) higher magnification, (ii)
9 kinematic two beam conditions with [200] or [220] diffraction vectors, (iii) high angles of tilt:
10 $\approx 35^\circ$, and (iv) dark-field conditions with γ' -superlattice reflections. Moreover, EDX-line
11 scans across both types of γ -precipitates, edge-on as well as in-plane ones, were performed
12 (see section 3).
13
14

15
16
17 Due to a slight dissolution of the γ' -matrix next to the γ -precipitates, the size of the
18 γ -pits exceeds that of the original γ -precipitates to some extent. The γ' -dissolution blunts the
19 edges of the γ -pits because atoms at edges are less strongly bound. Typically the slopes of the
20 blunted edges have the indices {011}. This will be detailed in sections 4.2 and 4.3. Moreover,
21 the strain in the γ' -matrix next to the γ -precipitates may enhance the γ' -dissolution. In the
22 standard (incident electron beam parallel to [001]) micrographs the γ -pits produce mass
23 thickness contrast. The strain in the γ' -matrix next to the not etched away parts of the
24 γ -precipitates may give rise to some strain contrast.
25
26
27
28
29
30

31
32 **4.1.1 Edge-on γ -precipitates.** Often the strongly bright mass thickness contrast generated by
33 edge-on γ -pits is surrounded by a region of weaker contrast. It is due to the above mentioned
34 dissolution of the γ -matrix, especially at the edges of the γ -pits, and perhaps to some strain.
35 The area of the original, i.e. not pasted together standard micrograph corresponds to about
36 $60(\mu\text{m})^2$ of the thin foil. In most cases this area is dominated by either the (100)- or the
37 (010)-family of edge-on γ -pits. In figure 2, about 60% of them belong to the (100)-family.
38
39

40
41 This dominance is probably caused by an elastic interaction between the γ -precipitates [4,28],
42 which gives rise to a growth selection. The interaction in turn is due to their lattice mismatch.
43
44

45
46 On the basis of their brightness three types of images of edge-on γ -pits are
47 distinguished in figure 2: (i) at A, (ii) at B, and (iii) at C. Tilting through high angles ($\approx 35^\circ$)
48 and taking micrographs under two beam conditions yielded the information communicated
49 below.
50

- 1
2
3
4
5
6
7
8
9
10
11
12
13
14
15
16
- (i) A: very bright; the edge-on γ -precipitate led to a deep γ -pit in at least one surface of the thin foil. A γ -precipitate which intersects both surfaces gives rise to pits in both of them. In the latter case even holes may appear.
- (ii) B: dark; the edge-on γ -precipitate lies entirely within the foil and does not contact either surface; there is only strain contrast due to the elastic distortion of the lattice planes. Since the γ - and the γ' -phase have nearly the same average atomic number (see section 3) there is hardly any mass thickness contrast.
- (iii) C: moderate brightness; the edge-on γ -precipitate led to a shallow γ -pit in one surface of the thin foil.

17
18
19
20
21
22
23
24
25
26
27
28

At A in figure 2, two parallel γ -pits are very close together; at D the two images are nearly in line. The intersections between the edge-on γ -precipitate at E with the two surfaces of the foil have different lengths. The longer one is evaluated. At F, two γ -pit images cross each other. In this case one edge-on γ -precipitate intersects the upper and one the lower surface of the foil. On the basis of detailed analyses of the strain contrast patterns it is concluded that the two γ -precipitates do not contact each other. At G, the images of two parallel edge-on γ -pits superimpose with the image of an in-plane one.

29
30
31
32
33
34
35
36
37
38
39
40
41
42
43
44
45
46
47
48

The full axes $2\alpha'_{ij}$ and $2\beta'_{ij}$ of the individual γ -precipitate images are measured by manually marking the γ -pits. The subscripts i and j refer to the number of the evaluated pasted together micrograph ($i \leq Z=9$) and to the number of the individual γ -precipitate ($1 \leq j \leq N_i$) in micrograph No. i , respectively. Great care is exerted to only allow for the strong central mass thickness contrast and to disregard the weaker one reaching out further. The [integer](#) exponents n and k are chosen individually for each γ -pit such that the superellipse drawn according to equation (1) follows the TEM image well. In most (96%) cases, $n=k=3$ yield a very good representation. The overall averages over n and k are 2.99 and 3.03, respectively. A total of 4889 edge-on γ -pits is evaluated, on an average about 100 per original micrograph (area: $\approx 60(\mu\text{m})^2$). As detailed below, the described procedures do not yield the true half-axes α_{ij} and β_{ij} of the γ -precipitates, but the apparent ones α'_{ij} and β'_{ij} .

49
50
51
52
53
54
55
56
57
58
59
60

The γ -precipitates were partially or entirely etched away (see section 3). Not only those of them produced contrast in the TEM whose centres lay within the thin foil (in-foil

1
2 γ -precipitates), but also those whose centres lay outside the foil (out-of-foil γ -precipitates),
3
4 however, not more than $(\alpha_{ij} - w)$ away from a surface of the foil. If and only if the depth of
5
6 the γ -pit marking the position of the γ -precipitate exceeds the minimum depth w , sufficient
7
8 contrast is obtained. At F, figure 2 shows the superimposed images of a (100)- and of a
9
10 (010)-edge-on γ -pit. The contrast of both of them is strong. As communicated above, there is
11
12 no contact between the two γ -precipitates. At least the depth of one γ -pit cannot exceed half of
13
14 the thickness t of the foil. In figure 2, t is 352nm. Rather shallow edge-on γ -pits were imaged
15
16 under standard [001]-conditions and after tilting through about 35° . Comparisons of these
17
18 images led to the conclusion that w is around $0.1 \cdot t$. Hence in all evaluations $0.1 \cdot t$ is inserted
19
20 for w . The effects of inserting alternative values for w will be discussed towards the end of
21
22 this section.

23
24 In the evaluations, it is assumed (i) that in-foil γ -precipitates are imaged with their true
25
26 half-axes α_{ij} and β_{ij} and (ii) that the γ -pit images of out-of-foil γ -precipitates yield chords
27
28 (see equations (3)). Hence in the case of $w=0$, on an average α'_{ij} and β'_{ij} of out-of-foil
29
30 γ -precipitates equal $\frac{1}{2}\sigma_\alpha(n)$ and $\frac{1}{2}\sigma_\beta(n,k)$, respectively. With the exception of γ -images of
31
32 type (ii) (see at B in figure 2) one does not know whether a given γ -image represents an
33
34 in-foil or an out-of-foil γ -precipitate. Therefore corrections are performed on the basis of
35
36 equations (4), which represent weighted averages over both types of γ -precipitates. The
37
38 weights are t and $[2(\alpha_{ij} - w)]$ for in-foil and out-of-foil γ -precipitates, respectively. The
39
40 factor 2 allows for the two surfaces of the foil.

$$41 \quad \alpha'_{ij} = \frac{t \alpha_{ij} + (\alpha_{ij} - w) \sigma_\alpha(n)}{t + 2(\alpha_{ij} - w)} \quad (4a)$$

$$42 \quad \beta'_{ij} = \frac{t \beta_{ij} + (\alpha_{ij} - w) \sigma_\beta(n,k)}{t + 2(\alpha_{ij} - w)} \quad (4b)$$

43
44 If n equals k , the ratios α'_{ij}/α_{ij} and β'_{ij}/β_{ij} are the same. The centres of all visible
45
46 γ -precipitates with $\alpha_{ij} \leq w$ lie within the thin foil. Hence $\alpha_{ij} = \alpha'_{ij}$ and $\beta_{ij} = \beta'_{ij}$ hold for
47
48 them. Inversion of the two above equations yields:
49
50

$$\alpha_{ij} = \frac{-(t - q_C(n, n) \pi w - 2\alpha'_{ij}) + \left[(t - q_C(n, n) \pi w - 2\alpha'_{ij})^2 + 4q_C(n, n) \pi \alpha'_{ij} (t - 2w) \right]^{1/2}}{2q_C(n, n) \pi} \quad (4c)$$

$$\beta_{ij} = \frac{\beta'_{ij} [t + 2(\alpha_{ij} - w)]}{t + (\alpha_{ij} - w) q_C(n, k) \pi} \quad (4d)$$

On an average, α_{ij} and β_{ij} are about 7% larger than α'_{ij} and β'_{ij} , respectively. $\sigma_\alpha(n)$ and $\sigma_\beta(n, k)$ represent average chords calculated for $w=0$. Hence it is not quite correct to insert them into equations (4): analogous average chords calculated under disregard of the outermost parts (of extension w) of the γ -precipitate should be used instead. Equations (4) overestimate the corrections slightly.

The depth of a γ -pit left behind by an out-of-foil γ -precipitate exceeds w if and only if the original position of the γ -particle centre was not more than $(\alpha_{ij} - w)$, $1 \leq i \leq Z=9$, $1 \leq j \leq N_i$, away from a γ' -surface. There are $Z=9$ pasted together micrographs and N_i images of edge-on γ -pits in micrograph No. i . Evidently large γ -precipitates are favoured. Therefore the weights Q_{ij} , which are proportional to $\{1/[t_i + 2(\alpha_{ij} - w)]\}$, are used in the calculations of the average half-axes a_i and b_i , averaged over micrograph No. i . This weighting procedure is analogous to that in equations (4).

$$a_i = \sum_{j=1}^{N_i} \alpha_{ij} Q_{ij} \quad (5a)$$

$$b_i = \sum_{j=1}^{N_i} \beta_{ij} Q_{ij} \quad (5b)$$

with

$$Q_{ij} = \frac{1}{S_i} \frac{1}{t_i + 2(\alpha_{ij} - w)} \quad (5c)$$

and

$$S_i = \sum_{m=1}^{N_i} \frac{1}{t_i + 2(\alpha_{im} - w)} \quad (5d)$$

Inserting the weights Q_{ij} is analogous to the weighting procedures performed for spherical particles [2,11]. However, presently no corrections are necessary for a deficient resolution of the TEM. Since the overlap of γ -images can easily be discerned no corrections for overlap have to be made either. Equation (2a) yields for the volume Ω_{ij} of the γ -precipitate with the indices ij

$$\Omega_{ij} = q_v(n,k) \pi \alpha_{ij}^2 \beta_{ij} \quad . \quad (5e)$$

The average volume V_i of edge-on γ -plates in micrograph No. i is given by

$$V_i = \sum_{j=1}^{N_i} \Omega_{ij} Q_{ij} \quad . \quad (5f)$$

Let A_i be the evaluated area of micrograph No. i and f_i the total γ -volume fraction. 'total' means that the in-plane γ -precipitates are included; this introduces the factor 1.5. Thus one obtains for f_i

$$f_i = \frac{1.5}{A_i t_i} \sum_{j=1}^{N_i} \Omega_{ij} \frac{t_i}{t_i + 2(\alpha_{ij} - w)} \quad . \quad (5g)$$

It is emphasised that the summation is carried out only over edge-on γ -pits. Due to the above mentioned predominance of one family of $\{001\}$ - γ -precipitates in each original micrograph, the factor 1.5 needs justification. The final result for the γ -volume fraction f is the average over $Z=9$ pasted together micrographs taken at various areas of six thin foils (see above). Hence any predominance averages out. To conclude the average aspect ratio R_i is defined

$$R_i = \sum_{j=1}^{N_i} \frac{\alpha_{ij}}{\beta_{ij}} Q_{ij} \quad . \quad (5h)$$

The final results for the half-axes a and b , the aspect ratio R , the volume V , and the total γ -volume fraction f are the weighted averages over a_i , b_i , R_i , V_i , and f_i , respectively, $1 \leq i \leq Z=9$. The weights are $(N_i / \sum_{m=1}^Z N_m)$. The results have been compiled in table 1. The statistical error limit quoted for a and b is the sum over the standard deviation of the respective average

and an allowance of 0.5% for the uncertainty of the magnification of the TEM. In the case of f , additional 10% are added for possible inaccuracies of the foil-thickness and 3% for uncertainties in tracing out A_i . Throughout the following, such sums of errors will be referred to as statistical error limits; they include no allowances for systematic errors, e.g. for misinterpretations of the contrast. The distribution functions $\Phi(\alpha_{ij}/a)$ and $\Phi(\beta_{ij}/b)$ are shown in figure 3. Again the weights Q_{ij} are used. The full widths at half maximum are 0.94 and 0.60, respectively. Both distributions can be very well fitted by a log-normal law. In figure 3(c), β_{ij} is plotted versus α_{ij} , no weighting procedure is performed for this latter diagram. Though the scatter of the data is rather wide, the aspect ratio $R_{ij} = \alpha_{ij}/\beta_{ij}$ is clearly seen to increase with α_{ij} for small and medium sized α_{ij} and to level off for large α_{ij} . Hence it is only of limited value to quote an overall average R . Since the strain energy of γ -precipitates increases approximately as β_{ij}^2 , β_{ij} of only few of them exceeds 40nm and the distribution function $\Phi(\beta_{ij}/b)$ is more narrow than $\Phi(\alpha_{ij}/a)$. For $\alpha_{ij} \leq 700\text{nm}$, the function $\beta_{ij}(\alpha_{ij})$ can be well represented by a polynomial:

$$\beta_{ij} = h_0 + h_1 \alpha_{ij} + h_2 \alpha_{ij}^2 \quad (6)$$

with $h_0 = 12.97\text{nm}$, $h_1 = 0.0772$, and $h_2 = -0.5463 \cdot 10^{-4}(\text{nm})^{-1}$.

‘[insert table 1 and figure 3 about here]’

The stability of the final results has been checked by trying alternative input values for n , k , and w . Setting all exponents n and k equal to 3.0 or varying w between 0.0 and 0.2 t (t =thickness of the foil) alters the results for a , b , V , and f only within their standard deviations.

The present number 4889 of evaluated edge-on γ -precipitates is probably higher than necessary. In former TEM-studies of spherical nano-scale particles, about 1000 of them were found to be sufficient [2]. Presently, however, there must be enough micrographs taken at different parts of the specimen to average out the above mentioned predominance of one family of $\{001\}$ - γ -precipitates; otherwise the final result for f is inaccurate.

Deleted: are perfectly

Deleted:

Deleted: Evidently the aspect ratio $R_i = \alpha_{ij}/\beta_{ij}$ increases with α_{ij} .

Deleted: Since the strain energy of γ -precipitates increases approximately as β_{ij}^2 , β_{ij} of only few of them exceeds 40nm and the distribution function $\Phi(\beta_{ij}/b)$ is more narrow than $\Phi(\alpha_{ij}/a)$.

1
2
3
4 **4.1.2 In-plane γ -precipitates.** In figure 2 four types of images of them can be distinguished:

5 (i) at H, (ii) at I, (iii) at J, and (iv) at K.

- 6
7
8 (i) H: There is only strain contrast due to the distortion of the lattice planes. This in-plane
9 γ -precipitate lies entirely deep within the foil and has no contact with either surface.
10 Therefore no etching effects can be discerned. Since the average atomic numbers of
11 the γ - and the γ' -phase are nearly the same, hardly any mass thickness contrast is
12 generated.
13
14 (ii) I: This situation is analogous to the edge-on one at D, but the two γ -precipitates have
15 grown together. As detailed below, both long half-axes α_{ij} are evaluated. This
16 γ -precipitate has no contact with either surface of the thin foil.
17
18 (iii) J: This γ -precipitate has been completely dissolved; hence no strain, but only mass
19 thickness contrast is visible. There is overlap of this γ -image with one of type (ii).
20 Etching of the strain field originally lying between the surface of the foil and an
21 in-plane γ -precipitate may raise the depth of its pit above the actual thickness of the
22 γ -precipitate.
23
24 (iv) K: This γ -precipitate has been partially etched away. Two γ -pits appeared; their
25 boundaries are, however, not sharp. The slopes of the upper γ -pit probably have strong
26 $\{111\}$ -components (see sections 4.2 and 4.3). $\{111\}$ -planes intersect the surface of the
27 specimen along $\langle 011 \rangle$ -directions. There is strain contrast due to the elastic distortion
28 of the lattice planes as well as mass thickness contrast. The slight constriction is
29 reminiscent of the edge-on view at D.
30
31
32
33
34
35
36
37
38

39 Part of the above information was gained from micrographs taken after tilting the foil through
40 high ($\approx 35^\circ$) angles or under kinematic two beam conditions. These in-plane γ -pit images
41 clearly show that the γ -precipitates are not standard rotational ellipsoids.
42
43
44

45 The average longer half-axis α_{ij} of in-plane γ -precipitates can be derived from such
46 micrographs. Only type (i) (H in figure 2) and type (ii) (I in figure 2) images are evaluated;
47 there are 899 of them. The superellipses are drawn in the middle of the dark contrast (see
48 figure 2, right small micrograph). They directly yield α_{ij} , not only the apparent axis α'_{ij} . No
49
50
51
52

weighting procedure as in equation (5a) is performed. This is actually not quite correct: since the γ -precipitates which produce these types of images, do not contact either surface, weights approximately proportional to $[1/(t_i - 2\beta_{ij})]$ would be appropriate. However, β_{ij} of in-plane γ -precipitates is not known. Since β_{ij} increases with α_{ij} (see figure 3(c)), the disregard of the weights favours small γ -precipitates and thus leads to a slight underestimate of 1-2% of the average half-axis a . Since the growth of each γ -precipitate is influenced by its neighbours, its two half-axes α_{ij} measured along [100] and [010] differ sometimes, e.g. at I in figure 2. Such a case has been mentioned in connection with the introduction of equation (2c). On an average the difference between the two half-axes α_{ij} of in-plane γ -precipitates amounts to $\pm 10\%$. Their arithmetic mean is used. This is analogous to the procedures described in section 4.1.1 for edge-on γ -precipitates: for them only one long half-axis α_{ij} was measured and averaged over all evaluated γ -precipitates. Presently the average geometric mean of the two half-axes α_{ij} is only 1.1% smaller than their arithmetic mean. Type (iii) and type (iv) images are not evaluated, because the respective results are very sensitive to the etch and to the choice of the minimum depth w . The final result for the half-axis $a_{\text{in-plane}}$ of in-plane γ -precipitates is the weighted average over all evaluated micrographs. The weighting procedure is analogous to that applied in the case of edge-on γ -precipitates (see section 4.1.1). The result is listed in table 1. Evidently $a_{\text{in-plane}}$ agrees within $\pm 2.6\%$ with its counterpart $a_{\text{edge-on}}$; this agreement is quite gratifying. The γ -volume fraction cannot be derived from in-plane γ -precipitates alone, because they yield no information about the shorter half-axis b .

The total number of evaluated in-plane γ -precipitates of types (i) and (ii) is 899. This number is compared with an estimate derived from edge-on γ -precipitates:

$$N_{\text{in-plane}} = \frac{1}{3} \sum_{i=1}^Z f_i (t_i - 2b_i) A_i / V_i \quad (7)$$

with f_i = total γ -volume fraction, V_i = average volume of a γ -precipitate, t_i = thickness of the foil, b_i = average length of the shorter half-axis, and A_i = evaluated area, $1 \leq i \leq Z=9$ = total number of pasted together micrographs. The averages are taken over A_i . This calculation yields $N_{\text{in-plane}}=946$, which agrees within $\pm 2.6\%$ with the above quoted experimental datum.

The difference is below the error limit $1/\sqrt{N_{\text{in-plane}}}$, which amounts to 3.3%. This good agreement proves the consistency of all evaluations and that the predominance of one {001}-family of γ -precipitates was effectively averaged out.

'[insert figure 4 about here]'

4.2 Scanning electron microscopy

High resolution FESEM images of a thin TEM-foil were recorded with secondary electrons (SE) at 10kV [on photographic film](#). The tilting angle of the foil was 0° for the standard micrographs, $\pm 5^\circ$ for stereo pairs, and $\pm 30^\circ$ for some special purposes. Figure 4 shows two micrographs: the edge-on γ -pits are typical, the shape of in-plane ones, however, often strongly differs from that in figure 4(b) (see below). The intensity I of the brightness in the positive prints is a monotonically increasing function of the SE intensity I_{SE} . The ratio I/I_{SE} is affected by the photographic processes applied to the negatives and prints. [However, the photographic processes are performed according to a standardised protocol; hence all recorded negative films and the prints made from these films transfer \$I_{\text{SE}}\$ into the brightness of the prints reproducibly.](#) I_{SE} strongly depends on [29]: (i) the angle between the incident electron beam and the normal of the SE emitting area, (ii) the inclination of this area relative to the SE-detector, and (iii) the thickness t of the foil; this, however, only if t is smaller than the range of the incident electrons. Moreover, I_{SE} is strongly enhanced at edges. Three extended regions are distinguished in figures 4(a) and (b):

Deleted: 8

Region (1): I is very low in the centres of the γ -pit images; in this region I of edge-on γ -precipitates vanishes.

Region (2): I is high.

Region (3): I is moderate.

Region (1) corresponds to the bottom of the γ -pit, from which – in the case of edge-on γ -pits – zero and – in the case of in-plane ones – less SEs than from the γ' -surface reach the detector.

Region (3) is the γ' -surface. These regions are also noticeable in the diagrams $I(x)$ and $I(y)$ shown in figures 4(d), (e), and (g). Based on stereo pairs (see figure 5) and on AFM data (see section 4.3) it is concluded that Regions (2) are plane and parallel to {011}-planes of the thin

1
2 foil. Its envisaged surface profile is sketched in figure (6). If the foil had been strongly etched
3 Regions (2) are sometimes parallel to {111} (see section 4.3). {111}-planes intersect the
4 (001)-surface of the specimen along <011>-directions. If etching of an in-plane γ -precipitate
5 just starts as at K in figure 2 or if the level of the γ' -matrix reaches the original bottom of the
6 in-plane γ -precipitate, the resulting γ -pit deviates from that in figure 4(b): the γ -pit becomes
7 nearly circular or changes its orientation. This will be discussed further in section 4.3.1. In the
8 case of edge-on γ -pits, Region (2) has a rather sharp edge at its lower end (see figure 6(a));
9 this edge gives rise to very high SE emission. In figure 4(a) this edge appears as a very bright
10 hem around Region (1) and in figures 4(d) and (e) this hem manifests itself in sharp peaks.
11 The superellipses of edge-on γ -pits are fitted at the maximum brightness of the bright hem
12 (see figures 4(a) and (c)). In-plane γ -pits will be discussed further in section 4.2.2. The
13 superellipses are drawn around them at the outermost edge of their bright contrast (see
14 figure 4(f)). In strongly etched specimens sometimes {001}-terraces interrupt the
15 {011}-slopes of edge-on γ -pits (see section 4.3.1).

16
17
18
19
20
21
22
23
24
25 '[insert figures 5 and 6 about here]'

26
27
28 Digitising of the photographic FESEM negatives and the numerical analyses were
29 analogous to those of the TEM images (see section 4.1), but zero was inserted for the
30 foil-thickness t and the minimum depth w . Since all four evaluated micrographs were taken at
31 different areas of the same TEM-foil, they were not pasted together. The magnification was
32 between 11,000 \times and 20,000 \times , hence each micrograph covered between about 10 and
33 30(μm)² of the thin foil. It is questionable whether the four evaluated FESEM micrographs are
34 really representative of the dispersion of γ -precipitates in the entire volume of the specimen;
35 this concerns primarily the very few (see section 4.2.2) in-plane γ -pit images. The same four
36 micrographs are evaluated for edge-on and for in-plane γ -pits.

37
38
39
40
41
42
43 **4.2.1 Edge-on γ -precipitates.** In total 63 edge-on γ -pits are evaluated. Due to this low
44 number statistics are rather poor and the error limits are high. The FESEM images directly
45 yield the chords $\sigma_\alpha(n,k)$, and $\sigma_\beta(n,k)$ defined in section 2. With the aid of equations (3b)
46 and (3c) the half-axes α_{ij} and β_{ij} of the γ -precipitate No. ij are calculated. With only one
47 exception the exponents n and k equal 3. The averages (over micrograph No. i) a_i and b_i of the
48 two half-axes, R_i of the aspect ratio, and V_i of the γ -volume are obtained as in section 4.1.1.

Deleted: s (1) and

Deleted: meet at

Deleted: ,

Deleted: which

Deleted: transition

Equations (5) are applied with $t_i=0$ and $w=0$. w is assumed to vanish because even a very shallow γ -pit yields contrast. The factor 2 in equations (5c) and (5d), which stands for the two surfaces of the thin foil, cancels. The total, i.e. edge-on plus in-plane, γ -volume fraction f_i is calculated from the fraction of the area A_i of the micrograph No. i covered by edge-on γ -pit images. Equation (5g) is replaced by

$$f_i = \frac{1.5}{A_i} \sum_{j=1}^{N_i} 2 \alpha'_{ij} \beta'_{ij} q_C(n, k) \pi \quad . \quad (8)$$

The area of the evaluated edge-on γ -pits follows from equation (3e). The final averaging procedures over the four micrographs are analogous to those described in section 4.1.1, but f_i is weighted by A_i instead of by N_i . The final results for the averages a , b , R , V , and f are listed in table 1. The quoted statistical error limits represent the standard deviations of the respective averages plus – in the case of a and b - 2% for inaccuracies of the magnification of the FESEM (see section 3) and - in the case of f - 6% accounting for uncertainties in tracing out A_i (see section 4.1). The agreement between the SEM edge-on data and the respective TEM ones is good: $a(\text{SEM})$ and $b(\text{SEM})$ are 8% smaller than $a(\text{TEM})$ and $b(\text{TEM})$, respectively. Consequently $V(\text{SEM})$ and $f(\text{SEM})$ are 24% and 19%, respectively, below their TEM-counterparts. $R(\text{SEM})$ is very close to $R(\text{TEM})$. The error limit $\sqrt{1/63}$ of $f(\text{SEM})$ amounts to 13%. With the only exception of $V(\text{SEM})$, the edge-on SEM results agree with the respective edge-on TEM ones within the statistical limits of error.

4.2.2 In-plane γ -precipitates. For reasons given above, the shape of the in-plane γ -pits is often rather poorly defined. Moreover, there are only 11 of them. Their evaluation is analogous to that of edge-on ones (see section 4.2.1). The apparent half-axes α'_{ij} of the imaged superellipses equal $[0.5q_C(n, n) \alpha_{ij} \pi]$ (see equation (3a)). With one exception the exponent n is 3. No weighting procedure as in equation (5a) is performed, because it would involve the shorter half-axis β'_{ij} , which is unknown. f_i is calculated with the aid of equation (8), but the factor 1.5 is replaced by 3.0 because – in the case of in-plane γ -precipitates - the summation allows only for one of the three families of $\{001\}$ - γ -plates.

Deleted: as

Deleted: and in-plane

Deleted: respective

1
2
3
4
5
6
7
8
9
10
11
12
13
14
15
16
17
18
19
20
21
22
23
24
25
26
27
28
29
30
31
32
33
34
35
36
37
38
39
40
41
42
43
44
45
46
47
48
49
50
51
52
53
54
55
56
57
58
59
60

The overall arithmetic mean a of the two long half-axes and the volume fraction f are listed in table 1. The weighting procedures and the derivations of the error limits are the same as in section 4.2.1. The result for a is in excellent agreement with the respective TEM edge-on one, the error limit, however, is high. $f(\text{SEM, in-plane})$ turns out to be much higher than $f(\text{TEM, edge-on})$. The reason is that the number $N_{\text{in-plane}}=11$ of FESEM imaged in-plane γ -pits happens to be exceptionally high. The statistical average number $\langle N_{\text{in-plane}} \rangle$ can be estimated on the basis of $N_{\text{edge-on}}=63$ of imaged edge-on γ -pits. The ratio of the fractions of area covered by edge-on and by in-plane γ -pits is 2.0 because there are two edge-on $\{001\}$ -families, but only one in-plane family. Allowing for the average aspect ratio $R_{ij}=7.8$ (see table 1) one expects $\sigma=N_{\text{edge-on}}/N_{\text{in-plane}}=2.0 \cdot 7.8=15.6$. Evidently the present ratio $63/11=5.7$ happens to be far below the expected one and $f(\text{SEM, in-plane})$ is very high. The error limit $\sqrt{1/N_{\text{in-plane}}} = \sqrt{1/11}$ of $f(\text{SEM, in-plane})$ alone amounts to 30%.

4.3 Atomic force microscopy

Magnetic force microscopy (MFM) will be discussed in section 4.4. Both AFMs (AFM1 and AFM2, see section 3) were operated in the tapping mode. They were alternatively equipped with both types of tips (Tip1 and Tip2, see section 3). Figure 7 is a TEM bright field image of a Tip2 before its use. Each standard individual AFM image covers $5\mu\text{m} \times 5\mu\text{m}$ of the TEM-thin foil and has 512×512 pixels. The acquisition time for the image was 10-20min. To get more in-plane γ -pits, micrographs were also taken at lower magnification: $15\mu\text{m} \times 15\mu\text{m}$ with 512×512 pixels each. The scan direction was chosen to be close to $\langle 011 \rangle$, not $\langle 001 \rangle$, because thus the shorter half-axes β'_{ij} of the superellipses could be measured more accurately. In sections 4.3 (AFM) and 4.4 (MFM) two coordinate systems are used: (x,y,z) are determined by the crystallographic axes of the specimen and (x',y',z') are the coordinates of the AFM scan. z' equals z throughout. $z'=z=0$ characterises the average level of the γ' -surface. In the case of AFM, x' and y' are parallel to the $[\bar{1}\bar{1}0]$ - and $[110]$ -direction, respectively. In the case of MFM, the orientation of the (x',y') -axes relative to the crystallographic axes varies from specimen to specimen (see section 4.4). A topography AFM image is presented in figure 8(a). [The difference in contrast between edge-on and in-plane \$\gamma\$ -pits is due to the fact that those areas which lie more than 52nm below the \$\gamma'\$ -surface are shown in white and only](#)

[edge-on \$\gamma\$ -pits reach to this depth](#). After subtraction of the background, neighbouring original micrographs were 'pasted together' in the computer (see section 4.1). Four TEM-foils were studied at both magnifications.

'[insert figures 7, 8, and 9 about here]'

Figure 9 shows an edge-on γ -pit imaged with AFM2 equipped with a supersharp Tip1. The magnification was high: 512x512 pixels covered $1\mu\text{m}\times 1\mu\text{m}$ of the TEM-thin foil. The lines of equal height clearly indicate the three regions defined in section 4.2: Region (1) – flat bottom, Region (2) – ascent / descent approximately parallel to $\{011\}$, Region (3) – γ' -surface. The transition between Region (1) and Region (2) is very well defined.

Basically the numerical evaluation procedures are analogous to those applied to the FESEM images (see section 4.2). However, the derivation of the apparent half-axes α'_{ij} and β'_{ij} from the [three-dimensional](#) numerical AFM output data $z'(x', y')$ requires detailed analyses of the three issues (i)–(iii) listed below. Whereas the contrast evaluated for TEM and FESEM images stems mainly from the lower parts of the etched γ -pits, the AFM yields information on their upper parts. This will be discussed below. It depends on the surface profile of the specimen which point of the tip is closest to the specimen during the AFM scan. This point may be in the outermost sphere-shaped end of the tip or in its pyramidal shaft. At the point of closest approach the slopes $\partial z'/\partial x'$ of the tip and of the specimen surface are the same [11,30]; here the scan is supposed to be along the x' -axis. The AFM computer registers the nominal coordinates (x', y', z') . If the tip were infinitely slender and not inclined (see section 3), (x', y', z') would represent the profile of the specimen exactly. The function $z'(x')$ actually registered in a linear scan depends on (i) the original shape of the γ -precipitate, (ii) the amount of γ' -matrix which dissolved next to the γ -precipitate, and (iii) the shape and inclination of the tip. Issues (i) and (ii) determine the shape of the γ -pit.

'[insert figure 10 about here]'

4.3.1 Edge-on γ -precipitates. Some AFM profiles $z(x, \text{sim})$ were computer simulated for edge-on γ -pits and Tip2 shown in figure 7. It is inclined by 10° relative to the normal of the

Deleted: 29

specimen; this agrees with the actual geometry of AFM2. The full width of the γ -pit equals the present average full smaller axis $2b=52.2\text{nm}$ (see table 1). In the simulations the scan direction is parallel to the x - (not x' -!) direction. In figure 10(a) the γ -pit/ γ' -matrix interfaces are exactly normal to the x -direction. The profile in figure 10(b) is similar, but the top edges of the γ -pit are blunted. Their slopes have the indices $\{011\}$. Such blunting is brought about by a partial dissolution of the γ' -matrix because atoms at sharp edges are less strongly bound (see section 4.1). The micrographs presented in figures 2, 4, 5, 8, and 9 clearly show such blunting, mainly in the direction of the smaller half-axis β_{ij} . Along the longer half-axis

α_{ij} blunting is less pronounced, moreover α_{ij} is close to $8\beta_{ij}$ (see table 1). Hence blunting causes hardly any problem in the determination of α_{ij} . Figure 10 shows the profiles $z(x, \text{sim})$. Due to the finite opening angle (half-cone angle: $\approx 12^\circ$) and the inclination of the tip, the maximum depth is 69nm and 124nm in figures 10(a) and (b), respectively. Because of the inclination of the tip the slopes of the right and left flanks of $z(x, \text{sim})$ are not the same.

If a foil had been very strongly etched, the slopes of the blunted edges do not have the indices $\{011\}$, but $\{111\}$, i.e. the most densely packed planes are exposed. $\{111\}$ -planes intersect the (001)-surface of the specimen along $\langle 011 \rangle$ -directions. This may give the outline of edge-on γ -pits a zigzag appearance and in-plane ones become approximately circular (see γ -pit C in figure 8(a)) or change their orientation (see γ -pit D in figure 8(a)).

In contrast to the computer simulated AFM-profiles $z(x, \text{sim})$ shown in figure 10, observations by AFM revealed that in Region (2) (see figure 6 and section 4.2) the ascents and descents of strongly etched specimens are terraced: the $\{011\}$ -planes are interrupted by horizontal (001)-planes (see figure 9(c)). The (001)-terrace in figure 9(c) extends over about 5 pixels. This result could be obtained neither by TEM nor by SEM. Due to these (001)-terraces the overall angles between the ascents, respectively descents, and the γ -surface are often less than 45° . Based on the results of the computer simulations and on analytical considerations the following procedures for obtaining the apparent half-axes α'_{ij} and β'_{ij} and the exponents n and k are adopted.

Determination of β'_{ij} : About seven (in the following this number will be referred to by the letter ν , $\nu \approx 7$) edge-on γ -pits of various sizes are chosen randomly in each original

Deleted: much

Deleted: $\nu \approx 7$

Deleted:

1
2
3
4
5
6
7
8
9
10
11
12
13
14
15
16
17
18
19
20
21
22
23
24
25
26
27
28
29
30
31
32
33
34
35
36
37
38
39
40
41
42
43
44
45
46
47
48
49
50
51
52
53
54
55
56
57
58
59
60

5 $\mu\text{m}\times 5\mu\text{m}$ micrograph and the profiles $z(x)$, respectively $z(y)$ (see figure (8b)), along the shorter axes are calculated from the $z'(x',y')$ -AFM data. For each of the $\nu \approx 7$ γ -pits, the z -level $\zeta_m < 0$, $1 \leq m \leq 2\nu$, is marked at which the slope $|\partial z / \partial x|$, respectively $|\partial z / \partial y|$, changes markedly. This change indicates the sharp transition from Region (1) to Region (2) sketched in figure 6(a) and defined in section 4.2. ζ_0 is the average over ζ_m , $1 \leq m \leq 2\nu$. The factor 2 before ν is due to the fact that each γ -pit has two slopes: ascent and descent. At the level $z = \zeta_0$, β'_{ij} is measured for all edge-on γ -pits in the considered $5\mu\text{m}\times 5\mu\text{m}$ micrograph. The standard deviation of ζ_0 within one original $5\mu\text{m}\times 5\mu\text{m}$ micrograph amounts to about 5%. Due to differences in etching, the scatter of ζ_0 found for different TEM-foils is larger: ζ_0 ranges from -40nm to -100nm . It is reiterated that etching was not intentional, but a mere side effect of the standard twin-jet electro-polishing procedure of TEM-foils. If etching had been geared to AFM, $|\zeta_0|$ would have been small and reproducible (see section 5). For $z < \zeta_0$, the slopes $\partial z / \partial x$ and $\partial z / \partial y$ are determined by the half-cone angle of the tip and its inclination. Those parts of the γ -pits which lie below the level $\zeta_0 = -52\text{nm}$, are white in figure 8(a).

Determination of α'_{ij} : As stated above, α'_{ij} can easily be measured. α'_{ij} is visually derived from those points in the micrographs (see figures 8(a) and (b)) where the contrast changes rapidly; this is analogous to the measurement of β'_{ij} , but there is no need to establish the profiles $z(x)$ and $z(y)$. The level $|z|$ at which α'_{ij} is measured, is about one half of $|\zeta_0|$ used for β'_{ij} .

Exponents n and k : Since α'_{ij} and β'_{ij} are determined at different levels z , n and k cannot be obtained by AFM. Based on the TEM results (see section 4.1.1), throughout the evaluations 3 is inserted for n and k .

Ten pasted together micrographs taken for four thin TEM-foils are evaluated; they contain 1829 edge-on γ -pits. The calculations are the same as described in section 4.2.1 for edge-on γ -pits imaged by FESEM. The only differences concern the calculations of the statistical limits of error: that of the magnification has been given in section 3 and that of the area A_i appearing in equation (8) is 4.5%. The final results are listed in table 1. The agreement

of the AFM results with the respective TEM ones is good. The average half-axes a and b are 11% below and 6% above the respective TEM data. The γ -volume fraction $f(\text{AFM, edge-on})$ is 17% smaller than $f(\text{TEM, edge-on})$. The average γ -precipitate volume $V(\text{AFM, edge-on})$ agrees within its statistical error limit with $V(\text{TEM, edge-on})$. The average aspect ratio $R(\text{AFM, edge-on})$ is 14% below $R(\text{TEM, edge-on})$; this difference reflects those concerning the half-axes a and b . There is no systematic dependence of a , b , or f on the AFM or on the tip used. The distribution functions $\Phi(\alpha_{ij}/a)$ and $\Phi(\beta_{ij}/b)$ are shown in figure 11. For comparison with the distributions determined by TEM for edge-on γ -precipitates (see figure 3), log-normal distribution functions are plotted in figure 11 with the *same* parameters as in figure 3. Evidently there is very good agreement between the distributions measured by AFM and TEM.

[insert figure 11 about here]

About every other pasted together area had to be disregarded because ζ_0 could not be accurately determined. About the same fraction of thin foils proved to be unsatisfactory for TEM work. Moreover, it must be kept in mind that one searches each foil already in the TEM for electron transparent areas and disregards thick ones. In the AFM investigation, however, areas with unsatisfactory γ -pits are only recognised during their evaluation. If the preparation of the present $\text{Ni}_{69}\text{Co}_9\text{Al}_{18}\text{Ti}_4$ -specimens had been geared to the AFM instead of to the TEM the fraction of good AFM images would have been higher.

Deleted: its value for

4.3.2 In-plane γ -precipitates. Three types of in-plane γ -pits are distinguished in figure 8(a):

(i) at B, (ii) at C, and (iii) at D.

(i) B: This γ -pit is similar to that marked K in figure 2, but that at B has been etched more strongly.

(ii) C: This γ -pit is rather shallow and approximately circular. Its ascents and descents have strong $\{111\}$ -components. $\{111\}$ -planes intersect the surface of the specimen along $\langle 011 \rangle$ -directions. The apparent longer half-axis α'_{ij} is measured along $\langle 001 \rangle$ -directions.

Deleted: near

(iii) D: Regions (2) (see section 4.2 and figure 6(b)) of this γ -pit are parallel to

{111}-planes. This γ -pit is very deep. α'_{ij} is measured along the $\langle 001 \rangle$ -diagonals.

Twenty-eight $15\mu\text{m} \times 15\mu\text{m}$ AFM-images are evaluated, they are not pasted together. The micrographs were taken for four different TEM-foils. A total of 402 in-plane γ -pits is evaluated. The half-axes α'_{ij} are measured as described in section 4.3.1. The further numerical evaluations are the same as in section 4.2.2. The results for the average longer half-axis a (AFM, in-plane) and for the γ -volume fraction f (AFM, in-plane) are listed in table 1. The error limit of the area A_i (see equation (8)) is 5%. The results agree satisfactorily with the respective edge-on TEM ones: a (AFM, in-plane) is 15% too high and f (AFM, in-plane) is 7% too low.

Deleted:

[insert figure 12 about here]

4.4 Magnetic force microscopy

As stated in section 3, AFM2 was equipped with a tip which had been coated with a 40nm thick hard magnetic cobalt alloy layer. As in section 4.3, the coordinate system (x', y', z') is that of the AFM scan and (x, y, z) is determined by the crystallographic axes of the specimen; z' equals z . Since the specimen had only been polished, but not etched ([see section 3](#)), it could not be orientated relative to the scanning direction by using the optical microscope attached to AFM2. Hence there is no general correlation between (x, y) and (x', y') . The tip and the specimen were magnetised with a small permanent magnet such that different poles meet during the measurements. Each line was scanned twice: first the profile $z'(x', y'=\text{const.})$ was registered in the standard tapping mode and subsequently the tip was raised to the level z_0 and scanned at the constant level z_0 , i.e. during the second scan the tip did not contact the specimen. The magnetic interaction of the tip with the specimen alters the resonant frequency of the cantilever and thus leads to a phase shift φ between it and the driving frequency. During the second scan, $\varphi(x', y'=\text{const.})$ was registered. In figure 12(a) a standard tapping mode topography $z'(x', y')$ -image and in figures 12(b), (d), and (f) $\varphi(x', y')$ -images are shown; φ varies between $+0.1^\circ$ and -0.15° . Since neither details of the magnetic properties of the γ - and γ' -phase nor of the tip are known, φ could not be calculated as a function of the shape and the size of the γ -precipitates. The same two areas A_1 and A_2 of one specimen were

1
2 evaluated for edge-on and in-plane γ -pits; A_1 consisted out of one and A_2 out of nine pasted
3
4 together $5\mu\text{m}\times 5\mu\text{m}$ micrographs. The error limit of A_i is 4.5%.
5
6

7 **4.4.1 Edge-on γ -precipitates.** In total there are 131 of them. The superellipses are drawn such
8 that they include the whole area in which φ is strongly negative, i.e. below some limit
9

10 $\omega_0 \approx -0.02^0$ (see figure 12(d)). ω_0 varies slightly with z_0 . On the basis of the TEM results
11 (see section 4.1.1) the exponents n and k are set equal to 3. A superellipse is outlined in
12 figure 12(d). The further evaluations follow those applied to the FESEM images of edge-on
13 γ -pits (see section 4.2.1). The results have been compiled in table 1. That for the longer
14 half-axis a (MFM) is in excellent agreement with that obtained by TEM, but the result for the
15 shorter half-axis b (MFM) exceeds b (TEM) by 48%. Consequently the average aspect ratio
16 R (MFM) is too low and the average volume V (MFM) too high. The volume fraction f (MFM)
17 in turn agrees perfectly with f (TEM). But since b (MFM) is much too high, the latter
18 agreement must be considered as fortuitous. The statistical error limit of f (MFM) amounts to
19 42%.
20
21
22
23
24
25
26

Deleted:

27 In spite of the low number of edge-on γ -precipitates studied by MFM and the
28 uncertainties concerning the interpretation of the φ -contrast, the result for a is surprisingly
29 accurate. The strong deviation of b (MFM) from the three other data listed in table 1 for b of
30 edge-on γ -pits, indicates systematic shortcomings of the present MFM evaluations. Since the
31 main components of the magnetic stray fields produced by edge-on γ -precipitates lie probably
32 in planes normal to them, the evaluation of a is expected to be far less critical than that of b .
33 Moreover, the smaller size of b makes it more sensitive to all types of errors.
34
35
36
37
38

39 **4.4.2 In-plane γ -precipitates.** There are only 20 of them. The superellipses are drawn at the
40 level $\varphi \approx -0.02^\circ$ (see section 4.4.1). An example is outlined in figure 12(f). The further
41 numerical evaluations are analogous to those performed for FESEM images (see section
42 4.2.2). The in-plane MFM results for the average longer half-axis a and for the γ -volume
43 fraction f have been compiled in table 1. a and f exceed the respective edge-on TEM results
44 by 11% and by 66%. Evidently the agreement concerning a is good. Hence the large
45 discrepancy concerning f must be due to errors in the number of evaluated in-plane γ -pits.
46
47 On the basis of the TEM investigations the ratio σ of the numbers of edge-on to in-plane
48 γ -pits is expected to be 15.6 (see section 4.2.2), which equals 2.4 times the present ratio
49
50
51
52
53
54
55
56
57
58
59
60

1
2 $\sigma=131/20=6.6$ (see section 4.4.1 and above). A possible reason why there were so many
3 in-plane γ -pits is that even those of them which lay entirely below the surface of the
4 specimen may have produced magnetic stray fields which were registered by the MFM.
5
6
7

8 5. Discussion

10 The microscopic characterisation of second phase particles involves two steps:

11 (i) generation of some contrast and (ii) relating it to the size and shape of the particles. In
12 most cases step (ii) is quite complex. One of the few exceptions are $L1_2$ -long-range ordered
13 γ' -precipitates embedded in the disordered γ -matrix of nickel based superalloys (see section
14 4.1): by TEM these γ' -precipitates are dark-field imaged with one of their superlattice
15 reflections. The difficulties encountered in measuring the γ' -volume fraction $f_{\gamma'}$ by AFM
16 have been demonstrated by Hazotte et al. [8], who determined $f_{\gamma'}$ of cuboidal γ' -precipitates in
17 an industrial nickel based superalloy. Their edge-length was about 500nm. The experimental
18 results for $f_{\gamma'}$ were found to decrease as the depth of etching increased. The correct value for
19 $f_{\gamma'}$ was obtained by extrapolating this depth to zero. Even in the relatively easy case of
20 dark-field TEM of spherical γ' -precipitates with average radii above 5nm, the error limit of $f_{\gamma'}$
21 is at best around 20% [2].
22
23
24
25
26
27
28
29
30

31 For the time being magnetic force microscopy is left aside; it will be discussed
32 towards the end of this section. The present plate-shaped γ -precipitates in $Ni_{69}Co_9Al_{18}Ti_4$ have
33 nearly the same chemical composition as the γ' -matrix and both phases have the f.c.c. crystal
34 structure. Hence in order to image the γ -precipitates by SEM and AFM, surface profiles had
35 to be generated. In the TEM these profiles yield mass thickness contrast and the γ -parts
36 remaining embedded in the γ' -matrix give rise to [some](#) strain contrast. The present surface
37 profiles were created unintentionally by etching during the standard electro-polish of thin
38 TEM-foils. Since the same specimens were meant to be investigated by TEM, SEM, and
39 AFM, their preparation had to be geared to TEM. During electro-polishing the γ -precipitates
40 dissolved faster than the γ' -matrix; hence γ -pits appeared (see section 3). The habit planes are
41 of the type $\{001\}$. The upper parts of the edge-on γ -pits are blunted: they are bounded by
42 $\{011\}$ -planes or – in the case of strongly etched specimens – by $\{111\}$ -planes (see sections
43 4.2 and 4.3). The contrast produced by the γ -pits was successfully related to the size and
44
45
46
47
48
49
50
51
52
53
54
55
56
57
58
59
60

1
2 shape of the γ -precipitates (see section 4). The procedures are different for TEM, SEM, and
3 AFM and for edge-on and in-plane γ -pits.
4

5
6 First edge-on γ -pits are discussed. The present description of the plate-shaped
7 γ -precipitates as superellipsoids turned out to be very convenient. All four relevant
8 parameters, i.e. the two average half-axes a and b and the two [average](#) exponents n and k
9 (equation (1)), can be derived from micrographs of edge-on γ -pits alone [25]. They also yield
10 the γ -volume fraction. For reasons given in section 4.3.1, n and k were presently not
11 determined by AFM. The contrast observed by TEM and SEM stems mainly from the deeper
12 parts of the γ -pits, whereas the AFM 'sees' only their surface-near parts. Therefore specimens
13 meant to be studied by AFM should be etched very lightly. In this case blunting of the γ -pits
14 is slight; hence the parameter ζ_0 introduced in section 4.3.1 is close to zero and the
15 exponents n and k can be determined by AFM.
16
17
18
19
20
21
22
23

Deleted: 4

24 The results obtained by TEM for edge-on γ -pits are considered as the most reliable
25 ones. The corresponding SEM and AFM results for the half-axes a and b and the γ -volume
26 fraction f agree well with the respective TEM data ([see table 1 and sections 4.2 and 4.3](#)). This
27 proves that AFM is well suited for the characterisation of nano-scale plate-shaped second
28 phase particles. No systematic shortcomings of this technique became evident. For spherical
29 particles analogous results were reported earlier [11,12].
30
31
32
33

34 Since the present preparation schedule had been geared to TEM, the AFM images had
35 to be evaluated as detailed in section 4.3.1. If, however, standard metallographic polishing
36 and etching procedures are carried out, the evaluations of AFM images can be automated.
37 This is a great advantage, especially in routine work. In contrast to TEM and SEM, AFM
38 images can be taken almost automatically. This compensates the advantage of the TEM,
39 which images many γ -pits and γ -precipitates simultaneously. Because of the abrupt changes
40 in the surface profile at the γ -pits, it is unlikely that the scan rates can be raised significantly
41 while a high resolution is kept. All procedures described in section 4 can also be applied to
42 particles which have the shape of cubes with rounded edges and corners. The only difference
43 is that the two half-axes α and β are the same. The γ' -precipitates in advanced nickel
44 based superalloys are such [rounded](#) cubes [2,7-9].
45
46
47
48
49
50
51
52
53
54
55
56
57
58
59
60

1
2
3
4
5
6
7
8
9
10
11
12
13
14
15
16
17
18
19
20
21
22
23
24
25
26
27
28
29
30
31
32
33
34
35
36
37
38
39
40
41
42
43
44
45

In-plane γ -pits yield only ancillary information: they show possible deviations of the plate-shaped γ -precipitates from a four-fold rotational symmetry around the shorter axis (see section 4.1.2). From *edge-on* γ -pits only the *average* longer half-axis is obtained. The present average difference between the two longer half-axes is, however, rather small: it amounts to only $\pm 10\%$ and the linear average over the two longer half-axes exceeds their geometric mean by only 1.1% (see section 4.1.2). Hence no appreciable error is made if the γ -volume fraction is derived from edge-on γ -pits alone.

14
15
16
17
18
19
20
21
22
23
24
25
26
27
28
29
30
31
32
33
34
35
36
37
38
39
40
41
42
43
44
45

The great advantage of magnetic force microscopy (MFM) is that no etching is needed. The applicability of MFM to the characterisation of second phase particles is naturally limited to materials for which the magnetic properties of the matrix and of the particles differ sufficiently. In spite of the present lack of information on the magnetic properties of the γ' - and the γ -phase and on the interaction of the MFM-tip with the specimen, all results obtained by MFM are acceptable; the result for the average longer half-axis of edge-on γ -pits agrees excellently with the respective TEM datum.

26
27
28
29
30
31
32
33
34
35
36
37
38
39
40
41
42
43
44
45

Most (96%) exponents n and k (see equation (1)) of the γ -plates in $\text{Ni}_{69}\text{Co}_9\text{Al}_{18}\text{Ti}_4$ equal 3. This expresses the observation (see figures 2, 4, 8, and 9) that the shape of the γ -precipitates deviates from that of a standard rotational ellipsoid with $n=k=2$ in three aspects: (i) the rim is less sharp, (ii) the large γ - γ' -interfaces which are approximately parallel to $\{001\}$, are nearly planar, and (iii) the cross sections of in-plane γ -precipitates deviate from circles towards squares. Their growth and thus their final shape are governed by the parameters listed at the beginning of section 1: specific interface energy, lattice mismatch, elastic stiffnesses, anisotropies, and precipitate volume. Only at the beginning of their growth, the γ -precipitates are of spherical shape. Later their lattice mismatch limits their growth along one $\langle 001 \rangle$ -direction and they become plate-shaped: they grow mainly at their rather blunt (see figures 2, 4, and 5) rim. Anisotropies of the stiffnesses and / or of the specific interface energy render the γ -plates nearly square-shaped.

46 6. Conclusions

- 47
48
49
50
51
52
53
54
55
56
57
58
59
60
1. The size, shape, and volume fraction of nano-scale plate-shaped second phase particles can be accurately measured by atomic force microscopy. The achieved accuracy is

1
2 comparable to that of transmission electron microscopy. In general slightly etching is
3 required.
4

- 5 2. If the magnetic properties of the nano-scale plate-shaped particles differ sufficiently
6 from those of the matrix, they can also be characterised by magnetic force microscopy.
7 In this case no etching is needed.
8

- 9 3. Nano-scale particles of any convex shape, e.g. γ' -cubes with rounded edges and
10 corners in nickel based superalloys, can be elegantly described as superellipsoids [25].
11 A superellipsoid is characterised by four independent parameters, all of which can be
12 measured in just one micrograph. With the aid of equations (1) – (3) all relevant
13 geometric parameters of such particles can easily be calculated.
14
15
16
17

Deleted: 4

18
19 ACKNOWLEDGEMENTS. The authors thank Mrs. A. Ricker (Institut für Medizinische
20 Physik und Biophysik) for technical assistance in the AFM work, Mrs. L. Rettich (Institut für
21 Materialphysik), and Mrs. G. Kieffermann (Institut für Medizinische Physik und Biophysik)
22 for photographic work. Financial support by the Deutsche Forschungsgemeinschaft and by the
23 research program MSM 0021620834 of the Ministry of Education of the Czech Republic is
24 gratefully acknowledged.
25
26
27
28
29
30
31
32
33
34
35
36
37
38
39
40
41
42
43
44
45
46
47
48
49
50
51
52
53
54
55
56
57
58
59
60

REFERENCES

- [1] A.J. Ardell, Metall. Trans. A **16** 2131 (1985).
- [2] E. Nembach, *Particle Strengthening of Metals and Alloys* (Wiley, New York, 1997).
- [3] J.L. Walter, M.R. Jackson and C.T. Sims (Editors), *Alloying* (ASM INTERNATIONAL, Metals Park, 1988).
- [4] A.G. Khachaturyan, *Theory of Structural Transformations in Solids* (Wiley, New York, 1983).
- [5] D.M. Barnett, J.K. Lee, H.I. Aaronson and K.C. Russel, Scripta Met. **8** 1447 (1974).
- [6] J.K. Lee, D.M. Barnett and H.I. Aaronson, Met. Trans. **8A** 963 (1977).
- [7] M. Göken and H. Vehoff, Scripta Mater. **35** 983 (1996).
- [8] A. Hazotte, M. Troyon and A. Bourhettar, Micros. Microanal. Microstruct. **7** 377 (1996).
- [9] M. Göken and M. Kempf, Acta Mater. **47** 1043 (1999).
- [10] K. Durst and M. Göken, Prakt. Metallogr. **38** 197 (2001).
- [11] U. Lagerpusch, B. Anczykowski and E. Nembach, Phil. Mag. A **81** 2613 (2001).
- [12] B. Fruhstorfer, V. Mohles, R. Reichelt and E. Nembach, Phil. Mag. A **82** 2575 (2002).
- [13] J. Wosik, H.J. Penkalla, K. Szot, B. Dubiel, F. Schubert and A. Czyska-Filemonowicz, Prakt. Metallogr. **39** 140 (2002).
- [14] W. Liu, H. Rösner and E. Nembach, Z. Metallkde. **88** 648 (1997).
- [15] T. Pretorius, D. Baither and E. Nembach, Acta Mater. **49** 1981 (2001).
- [16] D. Baither, T. Pretorius and E. Nembach, Acta Mater. **51** 1229 (2003).
- [17] F.R.N. Nabarro and M.S. Duesbery (Editors), *Dislocations in Solids*, Vol. 10 (Elsevier, Amsterdam, 1996).
- [18] R. Wagner and R. Kampmann, in *Materials Science and Technology*, Vol. 5, R.W. Cahn, P. Haasen and E.J. Kramer (Editors), (VCH Verlagsgesellschaft, Weinheim, 1991), p. 213.
- [19] M. Fähmann, W. Hermann, E. Fähmann, A. Boegli, T.M. Pollock and H.G. Sockel, Mater. Sci. Eng. A **260** 212 (1999).
- [20] D. Siebörger, H. Knake and U. Glatzel, Mater. Sci. Eng. A **298** 26 (2001).
- [21] P. Hein, Dansk Kunsthåndværk **37** 97 (1964).
- [22] L. Rosendahl, Appl. Math. Modelling **24** 11 (2000).

Deleted: 6

[23] A. Jaklic, A. Leonardis and F. Solina, *Computational Imaging and Vision*, Vol. 20

(Kluwer, Dordrecht, 2000), p. 13.

Formatted

[24] T. Wriedt, Part. Part. Syst. Charact. **19** 256 (2002).

Deleted: 3

[25] I. Sobchenko, J. Pesicka, D. Baither, R. Reichelt and E. Nembach, Appl. Phys. Letters, **89** 133107 (2006).

Deleted: 4

Deleted: in press

[26] E.W. Weisstein, *Superellipsoid* (MathWorld –A Wolfram Web Resource, 2006);

<http://mathworld.wolfram.com/Superellipsoid.html>.

Deleted: 5

[27] C.C. Jia, K. Ishida and T. Nishizawa, Metall. Mat. Trans. A **25** 473 (1994).

Deleted: 6

[28] M. Doi, Prog. Mater. Sci. **40** 79 (1996).

Deleted: 7

[29] L. Reimer, *Scanning Electron Microscopy*, second edition (Springer, Berlin, 1998).

Deleted: 8

[30] D. Keller, Surface Sci. **253** 353 (1991).

Deleted: 29

Table 1: Results for the half-axes a and b , the aspect ratio R , the volume V , and the volume fraction f (total, i.e. edge-on plus in-plane) of the γ -precipitates.

Statistical limits of error are quoted.

	TEM		SEM		AFM		MFM	
	edge-on	in-plane	edge-on	in-plane	edge-on	in-plane	edge-on	in-plane
a [nm]	209 ± 6	220 ± 6	192 ± 19	208 ± 40	185 ± 12	240 ± 17	211 ± 25	232 ± 17
b [nm]	26.1 ± 0.7	<i>J.</i>	24.1 ± 1.8	<i>J.</i>	27.7 ± 2.7	<i>J.</i>	39 ± 3	<i>J.</i>
R	7.8 ± 0.1	<i>J.</i>	7.8 ± 0.7	<i>J.</i>	6.7 ± 0.3	<i>J.</i>	5.4 ± 0.3	<i>J.</i>
V [10^6nm^3]	9.6 ± 0.7	<i>J.</i>	7.3 ± 1.5	<i>J.</i>	8.3 ± 2.0	<i>J.</i>	12.6 ± 2.8	<i>J.</i>
f	0.035 ± 0.008	<i>J.</i>	0.029 ± 0.008	0.075 ± 0.036	0.030 ± 0.004	$0.033 \pm .004$	0.036 ± 0.015	0.059 ± 0.016

FIGURE CAPTIONS

Fig. 1: Superellipsoids, the ratio α/β of the half-axes equals 5.0. Cross sections through the centre: (a) edge-on, (b) in-plane view. (c) Three-dimensional view. The exponents n and k are defined in equation (1); in (a) the parameter $q_v(n,k)$ (equation (2a)) is given below each sketch.

Fig. 2: Bright field TEM image of plate-shaped γ -precipitates and γ -pits in $\text{Ni}_{69}\text{Co}_9\text{Al}_{18}\text{Ti}_4$. The Miller indices of the plane of the thin foil are (001) and the electron beam is normal to it. The x - and y -axes are parallel to $\langle 001 \rangle$ -directions. Thickness of the foil: 352nm. For A - K see section 4.1. For one edge-on (L) γ -pit and one in-plane (H) γ -precipitate the superellipses are outlined; the magnification of these two small micrographs is 2.1 times that of the large one.

Fig. 3: Distribution functions (a) $\Phi(\alpha_{ij}/a)$ and (b) $\Phi(\beta_{ij}/b)$ of edge-on γ -precipitates measured by TEM. The dashed lines represent log-normal distributions functions fitted to the data. (c) β_{ij} is plotted versus α_{ij} , each point represents one γ -precipitate, \blacklozenge indicates the overall averages a and b and the curve shows equation (6). Less than about 0.5% of the data lie outside the ranges of the diagrams.

Fig. 4: High resolution FESEM secondary electron images of (a) edge-on and (b) in-plane γ -pits in $\text{Ni}_{69}\text{Co}_9\text{Al}_{18}\text{Ti}_4$. The x - and y -axes are parallel to $\langle 001 \rangle$ -directions. (c) The superellipse for γ -pit A is outlined, (d) intensity $I(x)$ of the brightness across A, (e) $I(y)$ across A, (f) superellipse for B, (g) $I(x)$ across B. I is in arbitrary units.

Fig. 5: Red-green anaglyph of an FESEM stereo pair of edge-on γ -pits. The stereo tilt angle is $\pm 5^\circ$.

Fig. 6: Schematic sketch of the surface profile at (a) an edge-on and (b) an in-plane γ -pit. The numbers indicate those of the 'Regions' defined in section 4.2.

Fig. 7: TEM bright field image of an AFM Tip2 before its use.

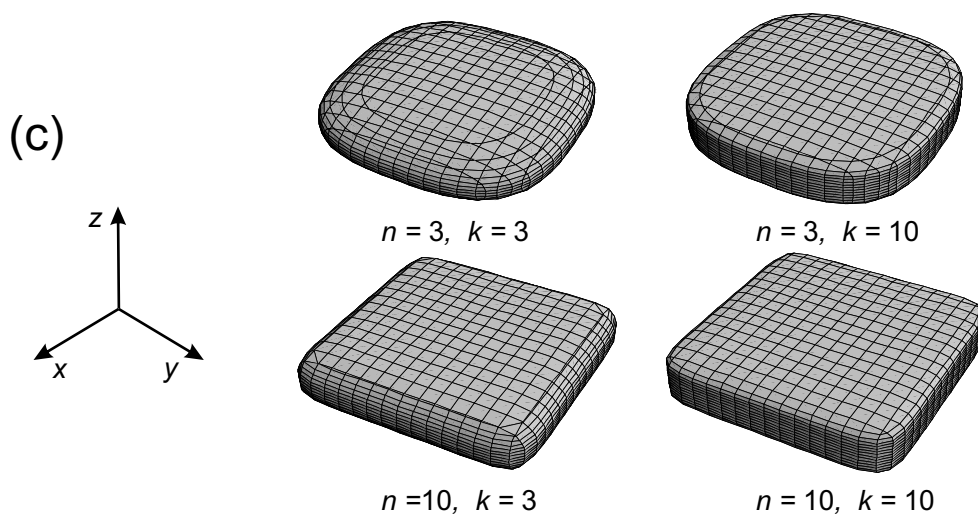
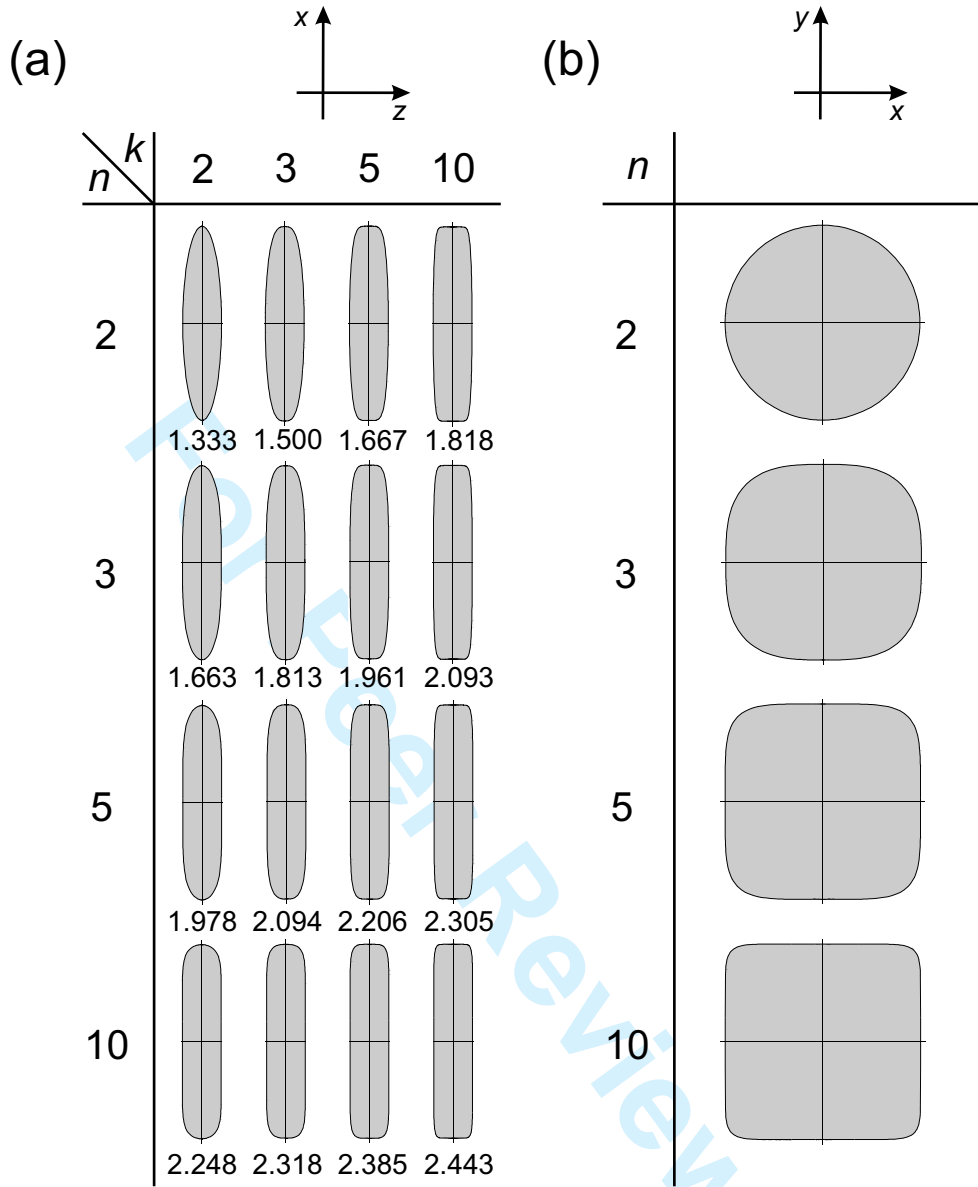
1
2
3
4 Fig. 8: (a) AFM (AFM2 with Tip2) topography image of γ -pits in $\text{Ni}_{69}\text{Co}_9\text{Al}_{18}\text{Ti}_4$. The x - and
5 y -axes are parallel to $\langle 001 \rangle$ -directions. Areas which lie deeper than $z = -52\text{nm}$, are shown in
6 white. The γ' -surface is at the level $z = 0$. A marks an edge-on γ -pit and B-D in-plane ones. (b)
7 Outline of the superellipse of the edge-on γ -pit A and its profile $z(y)$, (c) outline of the
8 superellipse of the in-plane γ -pit C and its profile $z(x)$.
9
10

11
12
13 Fig. 9: High magnification AFM (AFM2 with Tip1) topography image of an edge-on γ -pit.
14 Lines of equal height are indicated; the difference in height between neighbouring lines is
15 15nm. Areas which lie deeper than $z = -110\text{nm}$, are shown in black. The γ' -surface is at the
16 level $z = 0$. The arrow in (c) points at a (001)-terrace.
17
18
19

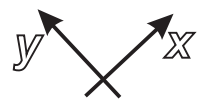
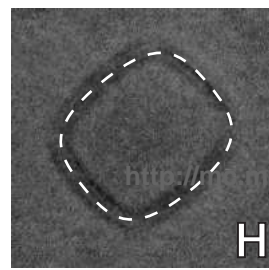
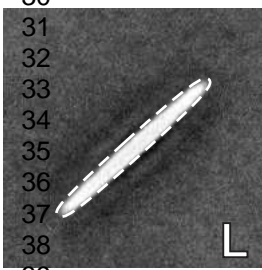
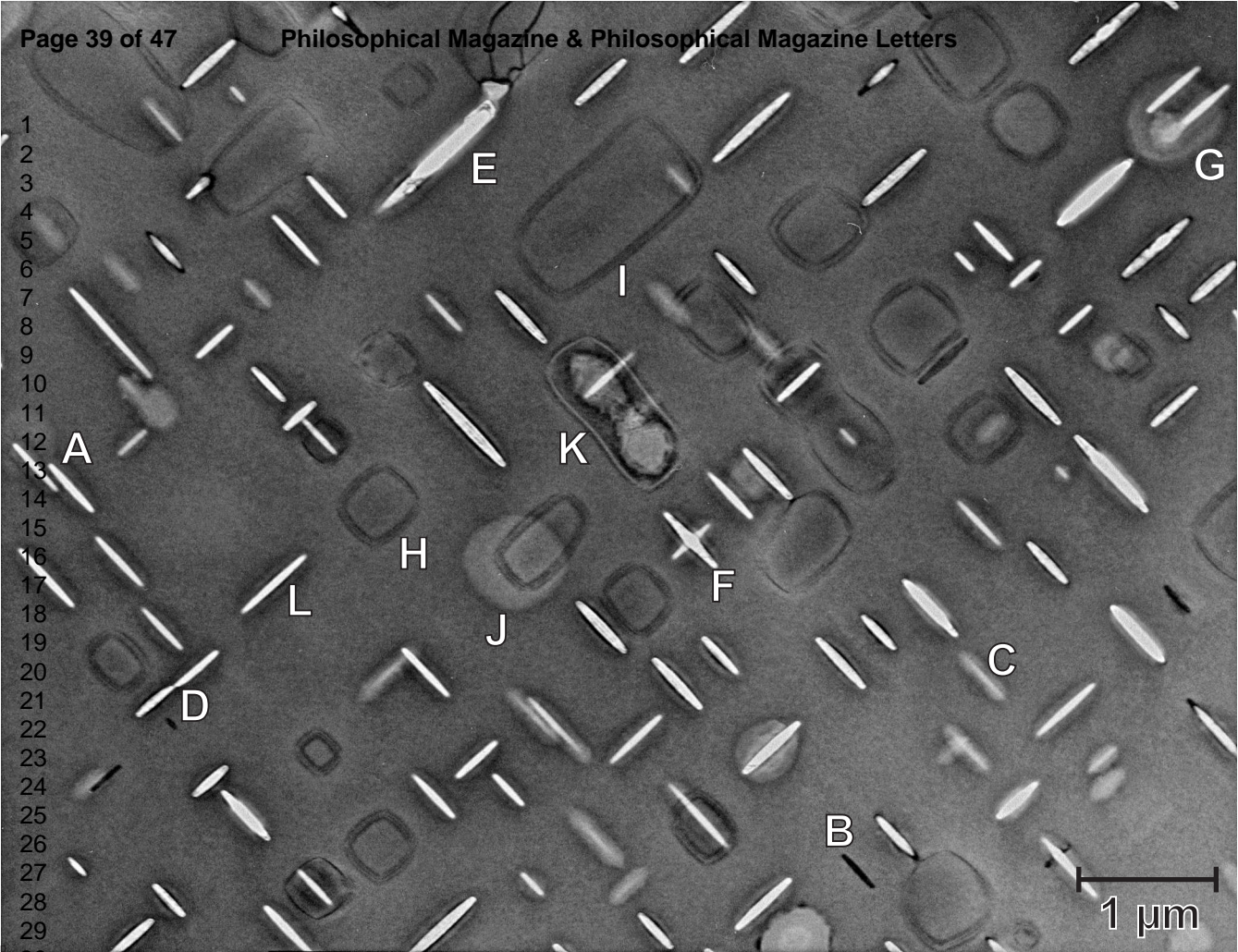
20
21 Fig. 10: Computer simulated surface profiles. The actual geometry of Tip2 (see figure 7) with
22 10° inclination is used. ——— Actual surface profile $z(x)$, - - - - simulated [AFM](#)-profile
23 $z(x, \text{sim})$.
24
25

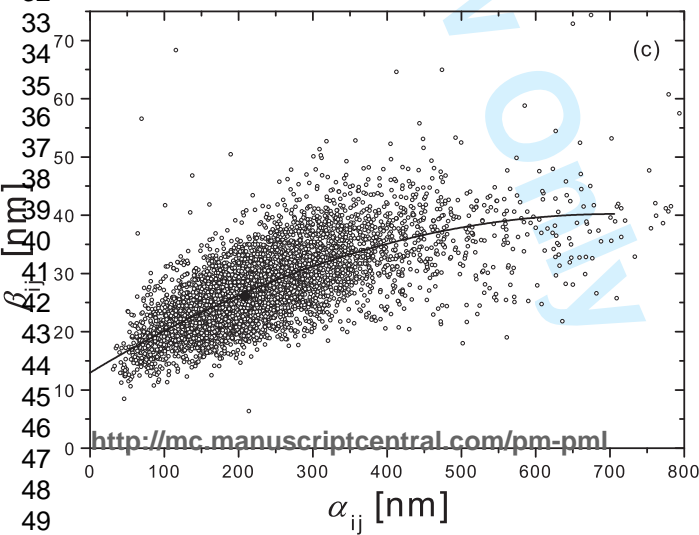
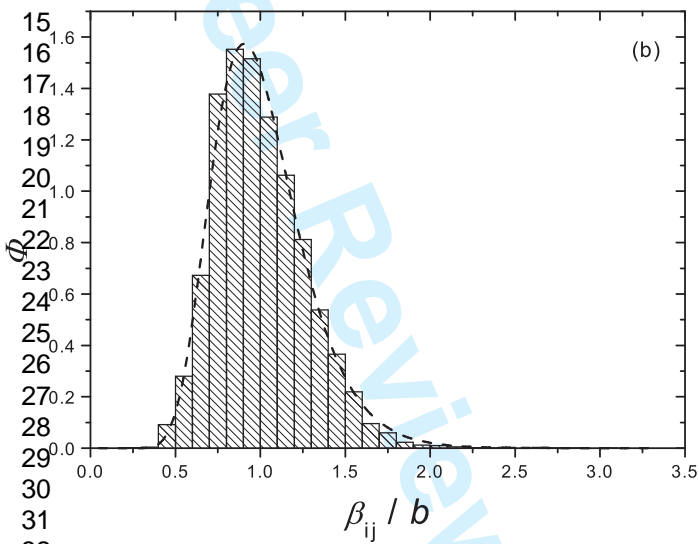
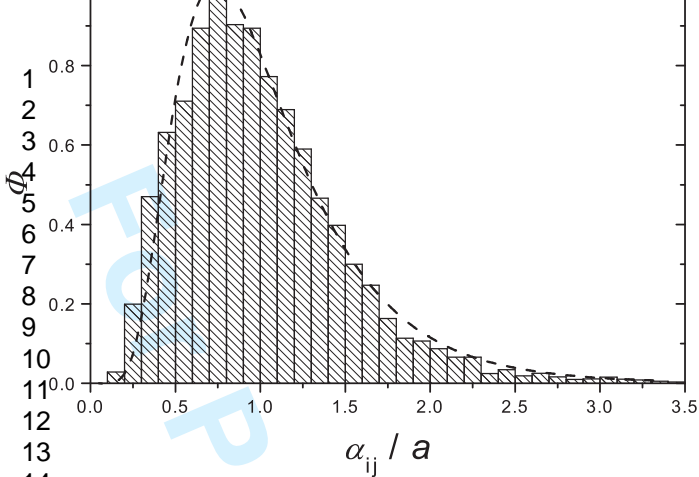
26
27 Fig. 11: Distribution functions (a) $\Phi(\alpha_{ij}/a)$ and (b) $\Phi(\beta_{ij}/b)$ of edge-on γ -precipitates
28 measured by AFM. The dashed lines represent the log-normal distribution functions fitted to
29 the TEM data (see figure 3).
30
31

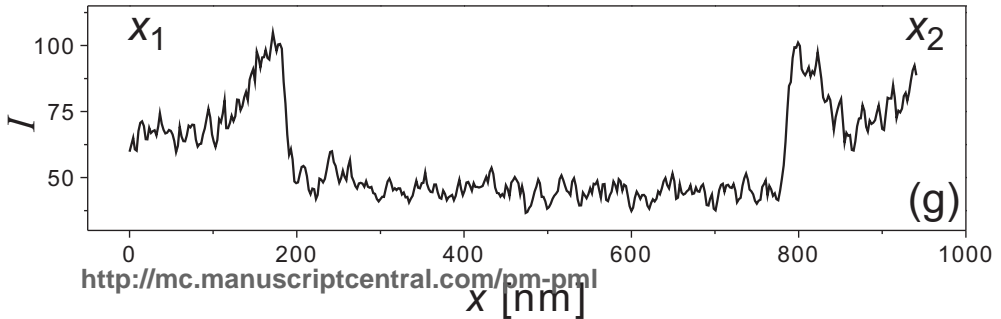
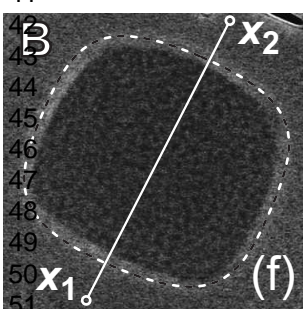
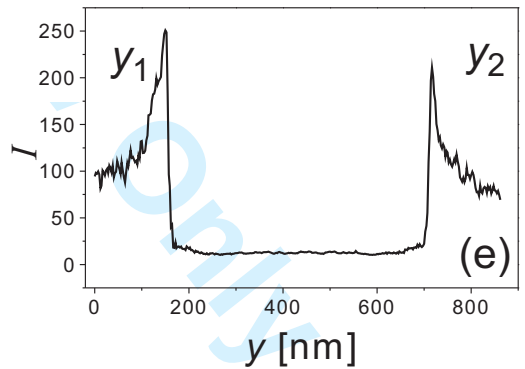
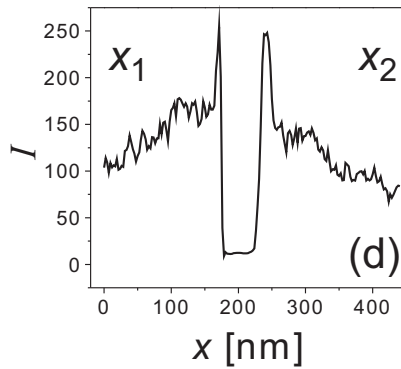
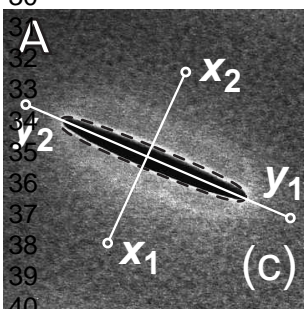
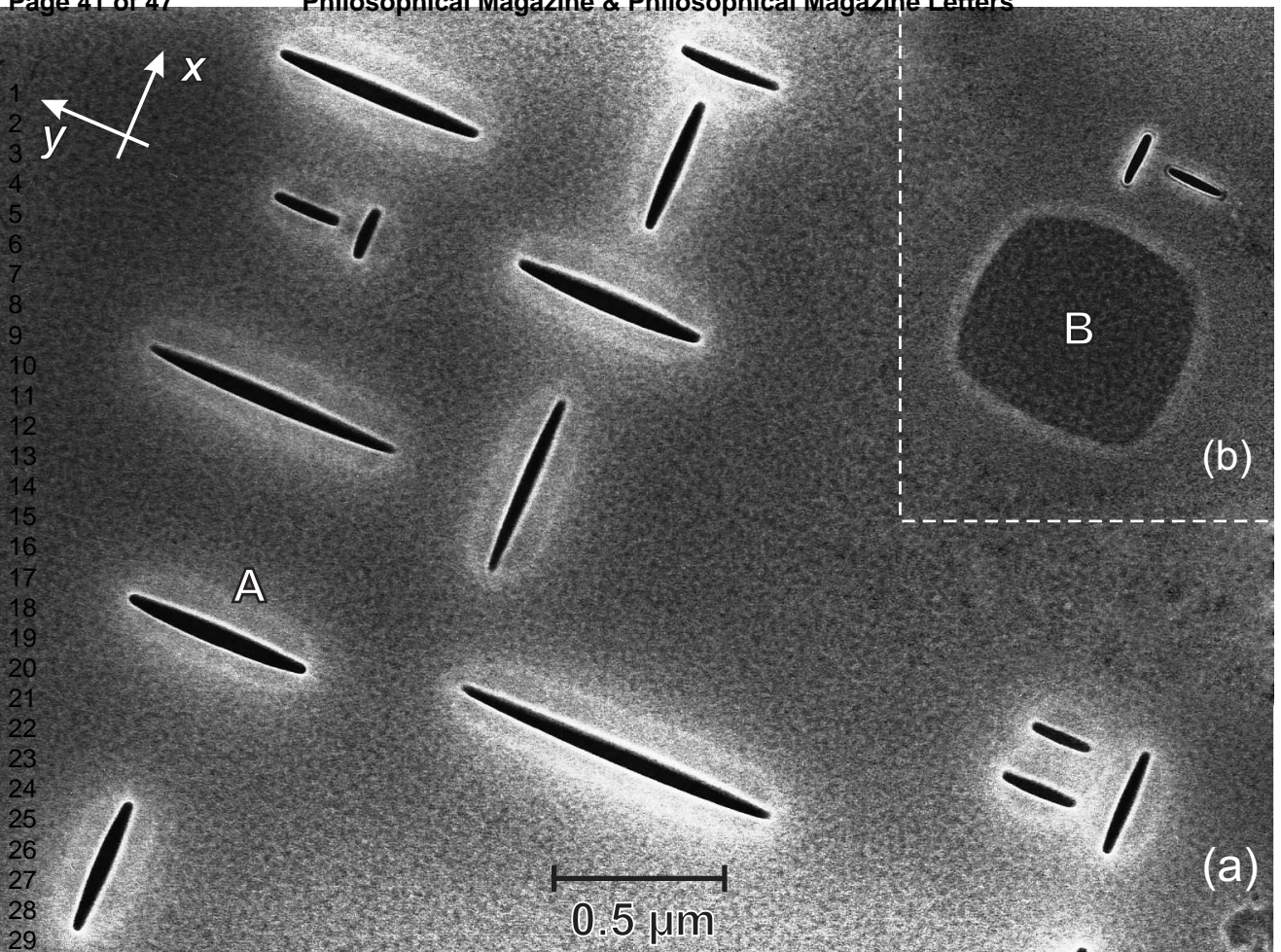
32
33 Fig. 12: (a,b) Images of a just polished $\text{Ni}_{69}\text{Co}_9\text{Al}_{18}\text{Ti}_4$ -specimen taken with AFM2 equipped
34 with a magnetic tip: (a) tapping mode, (b) φ -shift mode, the x - and y -axes are parallel to
35 $\langle 001 \rangle$ -directions. (c) Height-profile $z'(x')$ through (a). (d) Outline of the superellipse of the
36 edge-on γ -pit A in (b), (e) its profile $\varphi(x)$, (f) and (g) as (d) and (e), respectively, for the
37 in-plane γ -pit B in (b). Areas with $\varphi < -0.1^\circ$ are black in (b) and (d).
38
39
40
41
42
43
44
45
46
47
48
49
50
51
52
53
54
55
56
57
58
59
60



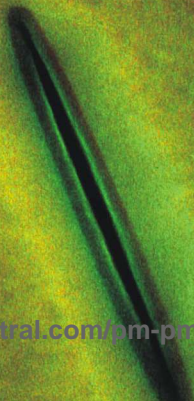
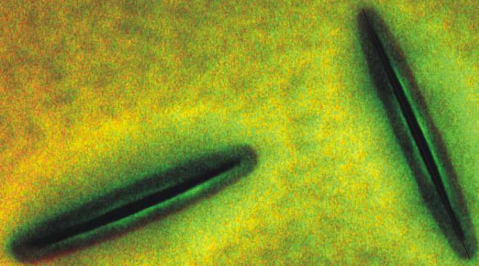
1
2
3
4
5
6
7
8
9
10
11
12
13
14
15
16
17
18
19
20
21
22
23
24
25
26
27
28
29
30







1
2
3
4
5
6
7
8
9
10
11
12
13
14
15
16
17
18
19
20
21
22
23
24
25
26
27
28
29
30



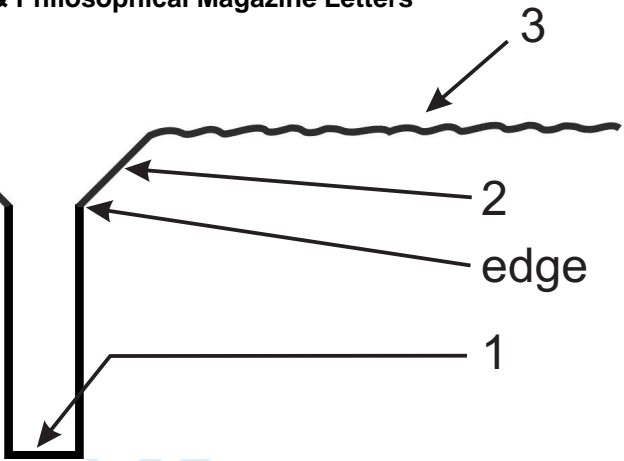
<http://mc.manuscriptcentral.com/pm-pml>
250 nm



(a)

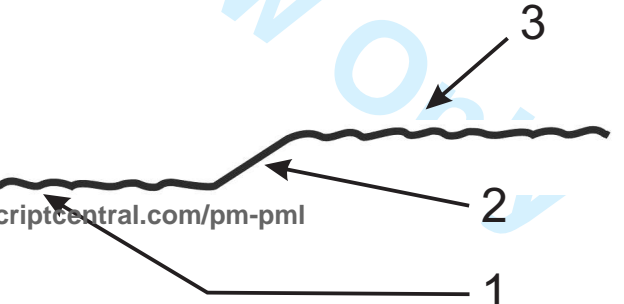
1
2
3
4
5
6
7
8
9
10
11
12
13
14
15
16
17
18
19
20
21
22
23
24
25

e^-
↓



(b)

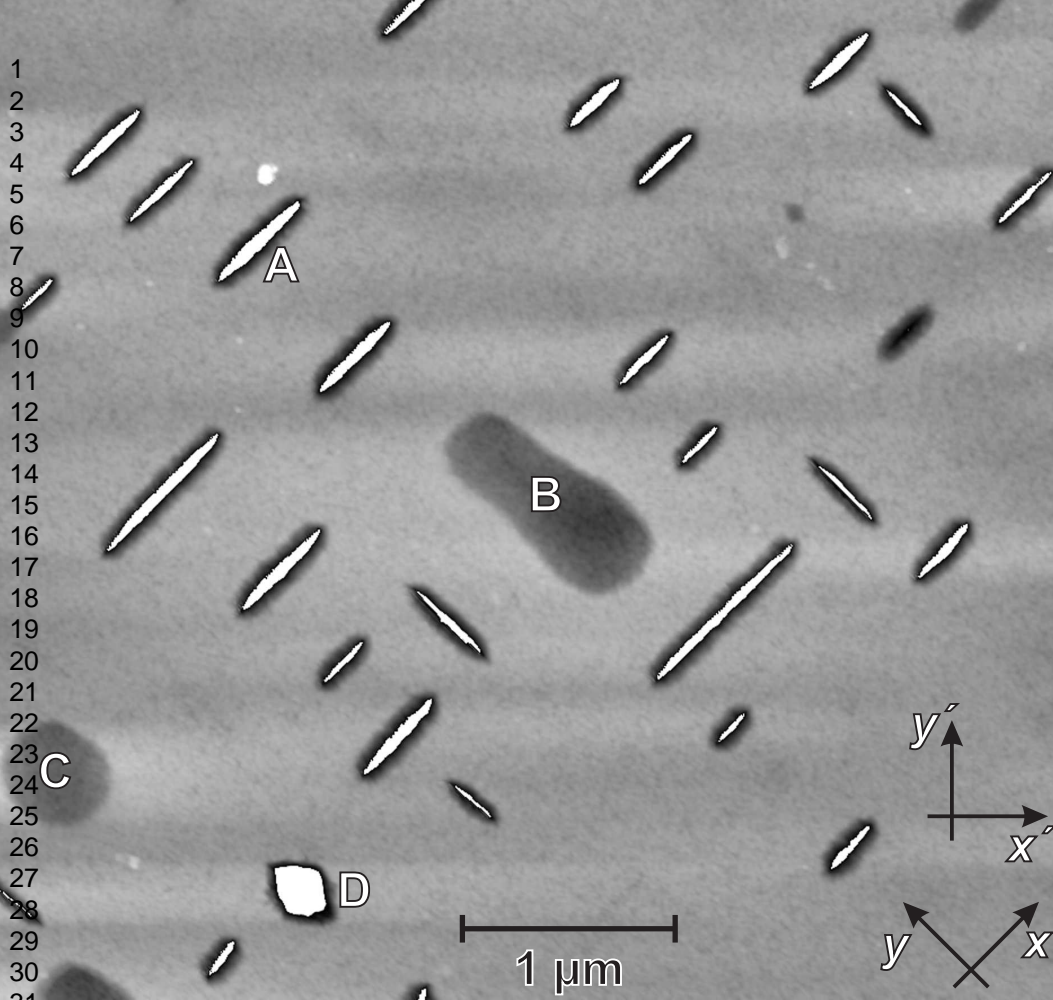
e^-
↓



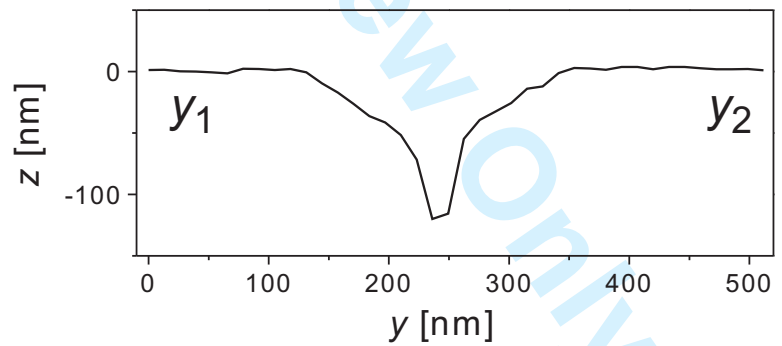
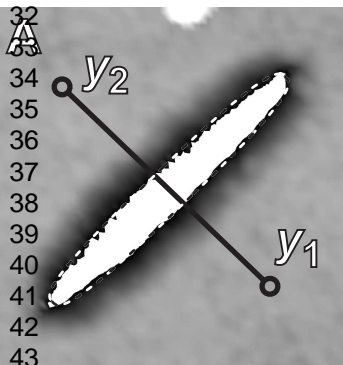
1
2
3
4
5
6
7
8
9
10
11
12
13
14
15
16
17
18
19
20
21
22
23
24
25
26
27
28

<http://mc.manuscriptcentral.com/pm-pml>

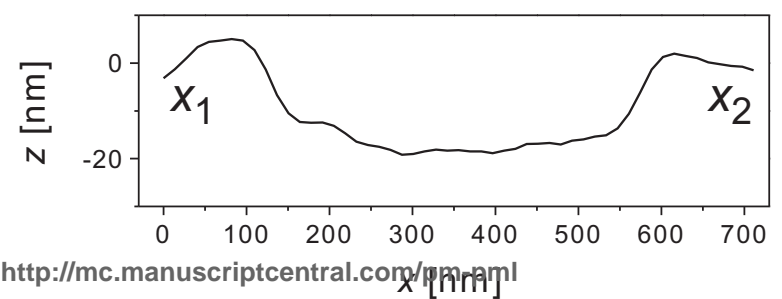
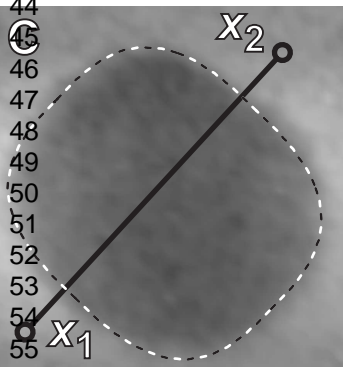
100 nm



(a)

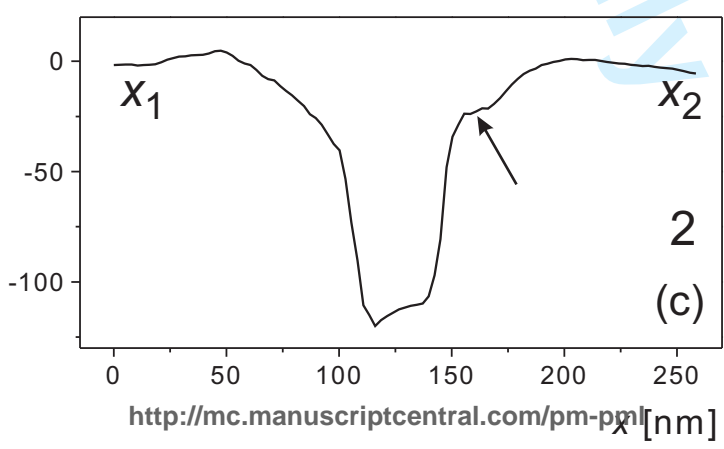
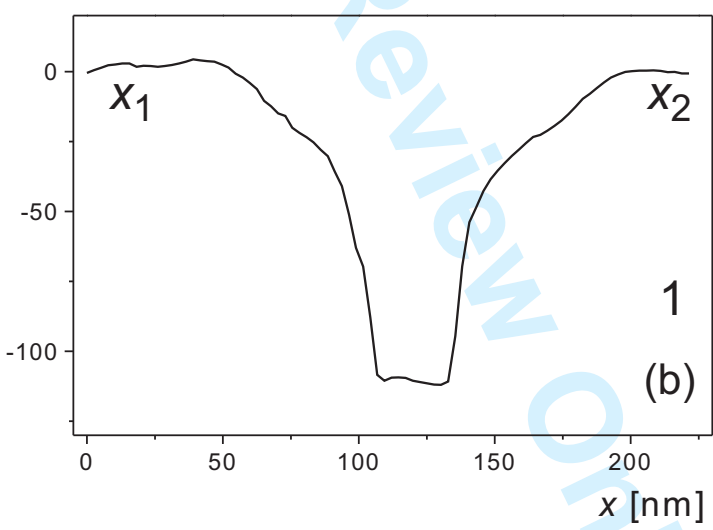
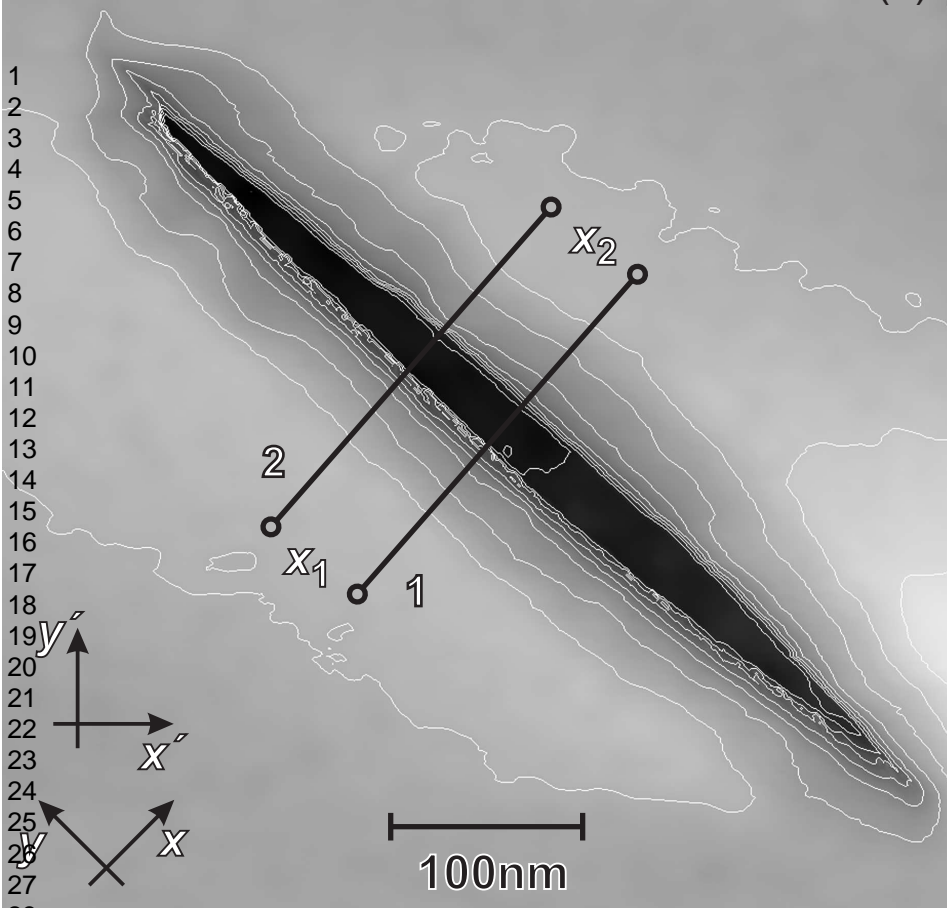


(b)



(c)

1
2
3
4
5
6
7
8
9
10
11
12
13
14
15
16
17
18
19
20
21
22
23
24
25
26
27
28
29
30
31
32
33
34
35
36
37
38
39
40
41
42
43
44
45
46
47
48
49
50
51
52
53
54
55
56
57
58
59
60



1
2
3
4
5
6
7
8
9
10
11
12
13
14
15
16
17
18
19
20
21
22
23
24
25
26
27
28
29
30
31
32
33
34
35
36
37
38